Remote Raman Spectroscopy. Profiling Water Vapor and Aerosols in the Troposphere Using Raman Lidars

D.D. Turner and D.N. Whiteman

Reproduced from:

Handbook of Vibrational Spectroscopy

John M. Chalmers and Peter R. Griffiths (Editors)

Remote Raman Spectroscopy. Profiling Water Vapor and Aerosols in the Troposphere Using Raman Lidars

D.D. Turner[1] and D.N. Whiteman[2]

[1] *Pacific Northwest National Laboratory, Richland, WA, USA*
[2] *NASA Goddard Space Flight Center, Greenbelt, MD, USA*

1 INTRODUCTION

Water vapor and aerosols are two important parameters in atmospheric science. They both participate strongly in processes that influence weather and climate and can be measured with high accuracy and high spatial and temporal resolution by Raman lidar.

1.1 Water vapor

Water vapor is the most important gas in the atmosphere, from a climatological point of view. Owing to its nature, it is one of the most active absorbers of infrared (IR) radiation, and thus is the most important greenhouse gas in the atmosphere. Water is the only substance that can exist in all three phases [gas, liquid, and solid (ice)] in the atmosphere, and readily changes phase at atmospheric temperatures. The latent heat involved in the condensation and evaporation of water vapor is a significant portion of the energy budget in the atmosphere. Clouds, which already contribute to the atmospheric energy budget through condensation and evaporation, also affect the radiative balance by reflecting incoming solar radiation and modulate the IR radiation emitted by the earth–atmosphere system to space depending on their location in the atmosphere. Water vapor is one of the most dynamic and variable gases in the atmosphere, with its total content ranging from nearly 0% to 4% of the total volume of the atmospheric column, depending on time and location.[1] Surface concentrations of water vapor decrease by more than an order of magnitude from the equator to the poles, and can change by 3–4 orders of magnitude in the vertical extent of the troposphere. At any given location in the atmosphere, the water vapor content can vary markedly in relatively short time spans owing to the passage of cold or warm fronts, precipitation, etc.

Because of the critical role that water vapor plays in most atmospheric processes, accurate water vapor profiles are needed in order for scientists to understand and model these processes better. Water vapor profiles are needed for basic meteorology applications (i.e. the identification and study of frontal boundaries, drylines, etc.), boundary layer studies (such as cloud formation/dissipation), development of climatological records, and for radiative transfer research. However, measurements of water vapor throughout the troposphere have proven to be difficult to make with good accuracy.

A wide variety of observational technologies have been developed to measure water vapor. Inexpensive in situ sensors have been installed on the ground and on towers and provide reasonably accurate water vapor measurements, but provide no information on the water vapor content of the atmosphere above these levels. In situ sensors have been installed on both commercial and research aircraft to measure water vapor. Water vapor measurements from commercial aircraft are a promising but yet unproven technique; however, they would only provide measurements when and where scheduled flights occur and thus the researcher might not have data where they are needed. Research aircraft

can provide high-quality measurements but the cost is high for dedicated aircraft flights. Another approach is to fly small in situ packages on balloons filled with helium or hydrogen. These packages, called radiosondes or rawinsondes (the latter measure profiles of wind direction and speed, in addition to the typical measurements of pressure, temperature, and water vapor), are fairly robust and provide a detailed vertical profile. However, the temporal resolution of the profiles is typically fairly coarse (the National Weather Service launches rawinsondes every 12 h at its launch sites). Moreover, radiosondes are expensive owing to manpower requirements. The absolute accuracy of radiosondes has also been questioned, owing to differences in measurements between radiosondes and other sensors in a variety of comparisons. Satellites can provide a global view of the water vapor distribution, but satellites make radiometric observations from which water vapor is retrieved [eg. Menzel *et al*.[2]]. Therefore, the radiative transfer models upon which the retrievals are built must be accurate and the retrievals themselves validated against some other measurement of the same parameter. Additionally, although satellites provide excellent global coverage, the horizontal resolution is typically fairly coarse, with the highest resolution being 1–4 km, and the vertical resolution is typically 1 km or more.

1.2 Aerosols

Aerosols, or small particles suspended in the atmosphere, are also dynamic and can influence the climate in a variety of ways. They can directly impact the atmospheric radiation budget by increasing the optical depth of the atmosphere or, to put it another way, by increasing the scattering and absorption of the incoming solar radiation such that less of this radiation reaches the surface. Aerosols also serve as cloud condensation nuclei, which are required for cloud droplet formation, and aerosols therefore have an indirect effect on the atmospheric radiation budget by moderating cloud formation processes and possibly cloud droplet optical properties. Aerosols in the atmosphere come from a variety of sources, both human-made and anthropogenic, including fossil fuel combustion, dust advected from the earth's surface, forest fires, volcanoes, and other sources. Aerosols can have a wide variety of physical and optical properties, depending on their composition, size, and other intrinsic factors.

Condensation of water vapor on atmospheric aerosol particles significantly affects the size, shape, and chemical composition of these particles, and therefore significantly affects the direct radiative forcing of the aerosols. Unfortunately, the technologies to provide profiles of aerosols are limited. A common technique currently used to profile aerosols is to fly in situ instruments on research aircraft (the instrumentation used to measure aerosols, such as nephelometers, absorption photometers, and optical counters, is too weighty and bulky to be flown as a small balloon borne package such as a radiosonde). However, like research-based water vapor instrumentation, these aircraft are too expensive to be flown regularly over an extended period of time.

To measure both water vapor and aerosol profiles routinely over long time periods, many research groups have turned to passive and active ground-based remote sensors. Passive ground-based remote sensors[3,4] are able to retrieve thermodynamic profiles with fair temporal resolution, but the vertical resolution remains coarse. However, active remote sensors are able to provide both high temporal and high spatial resolution needed for many research efforts. The development of the laser led to new active remote sensing technologies to measure both water vapor and aerosols. Shortly after the laser was invented, pulses of laser radiation were being transmitted into various media, such as the atmosphere, and the backscattered signal collected with a telescope as a function of time (and hence distance), in a manner that is analogous to radar. This new technique was called laser radar or lidar (light detection and ranging). There are many examples of "simple" lidars in atmospheric research that transmit laser energy and record the backscatter signal at the same frequency. These types of lidars have been and are being used to ascertain cloud base height (and cloud top height, if the laser beam is not attenuated by the cloud), the presence of aerosol layers, and other geophysical parameters. However, by carefully choosing the wavelength of the outgoing laser beam, or by observing the backscatter at wavelengths other than that of the laser, more information about the atmosphere can be obtained.

At present, the differential absorption lidar (DIAL) and Raman lidar are the most advanced remote sensing techniques to measure the vertical distribution of water vapor in the atmosphere with high temporal and spatial resolution. DIAL systems measure water vapor profiles by tuning the laser to a water vapor absorption line and then switching from this "on-line" frequency to a frequency where no water vapor absorption is expected (the "off-line" frequency). The two signals are then compared to derive the absorption due to water vapor and hence the water vapor density. DIAL systems are able to provide accurate high-resolution profiles of water vapor,[5] but require much more complex laser transmitters than Raman lidars, hence only experimental systems have been developed to date. Raman lidars have a relatively simple laser transmitter compared with DIAL systems, which makes the automation of the Raman lidar an easier feat. Water vapor Raman lidars simultaneously observe the backscatter due to Raman scattering of water

vapor and nitrogen molecules. At a given location, the ratio of the Raman water vapor signal to the Raman nitrogen signal is directly proportional to the absolute amount of water vapor in the atmosphere. An additional benefit is that the signal from the Raman scattering of nitrogen is a purely molecular signal, unlike the backscatter that is observed at the laser's wavelength, and can be used to derive profiles of aerosol extinction coefficient, an important optical parameter needed for aerosol research. Grant[6] gives a review of the two "competing" techniques, and efforts are under way to evaluate resolutions, accuracy, and available range of state-of-the-art water vapor Raman lidar and DIAL systems.[7,8]

Raman lidars have been used for a broad range of remote sensing applications. This article first briefly outlines the history of Raman lidars, and attempts to provide an overview of the broad range of applications of this remote sensing technique. We then briefly discuss the theory of water vapor and aerosol retrievals from Raman lidars. Subsequently, the details of an automated state-of-the-art water vapor and aerosol Raman lidar are presented. A variety of examples of data from this particular system are then shown and discussed to illustrate how the atmospheric community is using Raman lidar data.

2 RAMAN LIDAR HISTORY AND OVERVIEW

2.1 History of the Raman effect

In 1921, Chandrasekhara V. Raman and his students began to investigate the light-scattering properties of various substances.[9] Their experiments were carried out at the University of Calcutta in India where Raman held an endowed chair in Physics. These investigations led to the discovery of a very weak type of secondary light that is generated at wavelengths shifted from the incident wavelength. In their first efforts, they used filtered sunlight as the source and the shifted wavelengths were observed visually. Raman realized quickly that they were observing a completely new scattering phenomenon of fundamental importance.

In order to actually measure their results, they used a mercury arc lamp and a spectrograph to record the spectrum of the scattered light. They tested various transparent substances including solids, liquids, and gases and found that the scattered spectrum contained lines in addition to the lines in the mercury lamp. If sufficient intensity was used, each of the lines in the mercury spectrum gave rise to its own modified scattering. They found that the frequency shifts, their relative intensities, and the state of polarization were independent of the incident radiation.

Raman made the first announcement of these results in 1928 in Bangalore, India. He drew attention to the universality of the phenomenon and to the utility of the technique for characterizing the chemical identity of the scatterer since the frequency shifts were unique to the substance doing the scattering. He demonstrated that the frequency shifts of the scattered radiation in many cases agreed well with the frequencies of IR absorption bands of the same substances. Thus the frequency shifts observed were attributed to the frequencies of oscillation of the atomic bonds in a molecule. Raman was awarded the Nobel Prize for his work in 1930.

Raman scattering has been used to great effect in laboratory studies of various materials. Since the advent of the laser, it has also been used for atmospheric studies. After an introduction to optical remote sensing, some of those applications will be described.

2.2 Optical remote sensing and lidar

The laser revolutionized the field of optical remote sensing, but it should be noted that studies of optical backscattering from the atmosphere occurred prior to the invention of the laser. In the 1930s, Hulburt used mechanically chopped searchlights as an optical source and a telescope as a receiver to measure atmospheric signals to 28 km.[10] In the 1950s, Elterman derived atmospheric temperature to altitudes in excess of 60 km using the searchlight technique as well.[11] The use of searchlights continued into the 1960s until the laser was available as a replacement optical source.

Lidar measurements were made possible by the invention of the laser in 1960 by Theodore Maiman.[12] This early laser was based on a flashlamp-pumped ruby rod. Smullin and Fiocco performed the first laser remote sensing measurements using such a laser in May 1962 when they recorded laser echoes from the moon.[13] However, the real advance in laser remote sensing came with the invention of the Q-switch in 1962 by McClung and Hellwarth.[14] The addition of a Q-switch to a laser allowed the population inversion in the lasing medium to build up to much higher levels than was previously possible, resulting in greatly increased instantaneous power levels. With the availability of higher peak powers, the first laser remote sensing atmospheric studies followed quickly. In 1963, Fiocco and Smullin reported measuring high-altitude density layers in the atmosphere.[15] Significant early advances in lidar include the first DIAL measurements of water vapor in 1966[16] and the first measurements of the atmospheric sodium layer by resonant scattering in 1968.[17]

2.3 Raman lidar

It did not take long before researchers were attempting to use the Raman effect to study molecular species in

the atmosphere. The Raman lidar technique that developed from these early efforts entails measuring the rotational or vibrational–rotational component of Raman scattering from the atmosphere using a telescope as a receiver. This approach has proven to be a highly versatile one, permitting a variety of atmospheric studies. The range of possible measurements will now be illustrated using several examples.

2.4 The first measurements: nitrogen and oxygen

The first reported Raman lidar measurements from the atmosphere were of molecular nitrogen by Cooney in 1966 using a ruby laser (694.3 nm) and interference filters.[18] Leonard produced definitive measurements of Raman scattering from both N_2 and O_2 in 1967 using a nitrogen laser and tilting the filters to scan through the different Raman features.[19]

2.5 Pollution monitoring

Inaba and Kobayasi made early use of the spectroscopic power of the Raman effect for atmospheric studies with a mobile Raman lidar for pollution monitoring.[20,21] Their early system was based on a 0.3-m telescope and a Q-switched ruby laser (694.3 nm). This laser was later replaced by a pulsed N_2 laser (337.1 nm). The shorter wavelength was preferred owing to the frequency to the fourth power dependence of the Raman cross-sections. They used a single monochromator, box-car averager and an $X-Y$ plotter to record the results. Samples were taken at a range of approximately 30 m. Measurements were made in the ordinary atmosphere (Figure 1), oil smoke (Figure 2), and automobile exhaust (not shown). The measurements in the ordinary atmosphere showed the presence of the strong Rayleigh and Mie signal, in addition to returns from CO_2, O_2, N_2, and H_2O. In the oil smoke and automobile exhaust, liquid water was observed along with NO, CO, H_2S, and various hydrocarbons. The clear presence of various chemical species in these figures demonstrates the broad range of measurement capability of a Raman lidar. Commercial, mobile pollution-monitoring systems have also been constructed.[22]

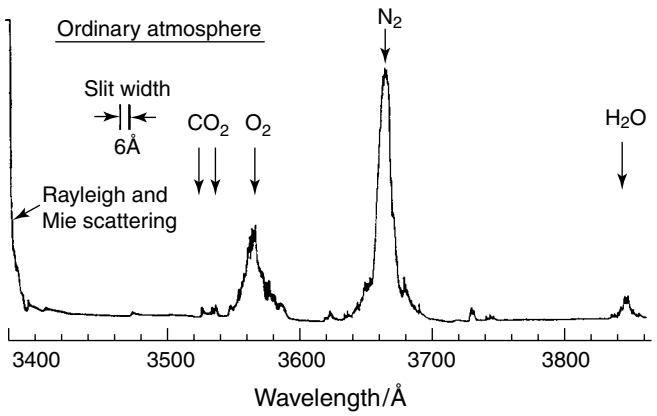

Figure 1. Measured spectrum of Raman-shifted and unshifted backscatters from the ordinary atmosphere. (Reproduced by permission of Kluwer Academic from Inaba and Kobayasi.[21])

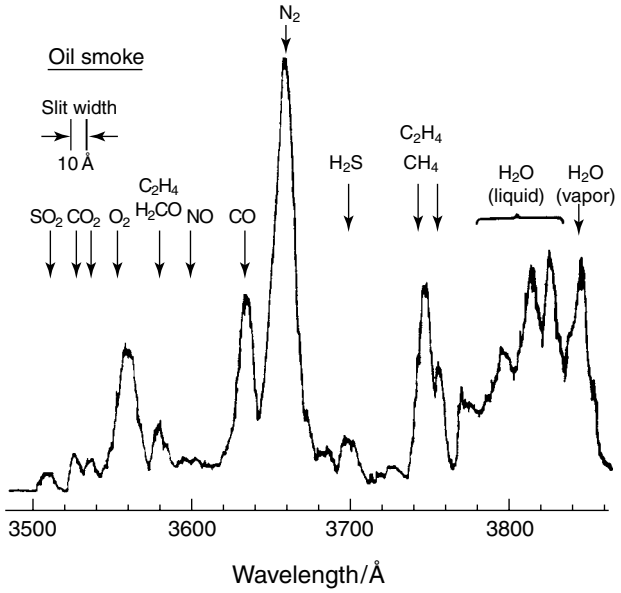

Figure 2. Spectral distribution of Raman-shifted components from a variety of molecular species in an oil smoke plume remotely analyzed by the laser-Raman method. (Reproduced by permission of Kluwer Academic from Inaba and Kobayasi.[21])

2.6 Water vapor

The great importance of water vapor in atmospheric studies led to early efforts to use the Raman lidar technique to measure it. Melfi *et al.*[23] and Cooney[24] separately measured Raman scattering from water vapor in 1969. Both used a frequency-doubled ruby laser (347.1 nm) for their measurements. Attempts to quantify the absolute amount of water vapor from these early measurements were hampered by the poor knowledge of the Raman scattering cross-section of water vapor. There are no known measurements of the Raman water vapor cross-section prior to the use of a laser.[25] The earliest reported values of the cross-section of water vapor seem to be those by Derr and Little where they stated that the Raman water vapor cross-section, when stimulated by 337.1-nm radiation, is $1.86 \times 10^{-29}\,\mathrm{cm^2\,sr^{-1}}$.[26] They gave no reference for this value, however. Currently, the best estimate of this cross-section is approximately $6 \times 10^{-30}\,\mathrm{cm^2\,sr^{-1}}$, given by Penney and Lapp.[27]

Owing to the lack of laboratory measurements of the water vapor cross-section, the early water vapor lidar measurements were used to determine this value, or more exactly to determine the value of the ratio of Raman water vapor and nitrogen cross-sections. Cooney obtained a value for this ratio of $5.1 \pm 75\%$ (which at 337.1 nm implies a Raman water vapor cross-section of $1.5 \times 10^{-29}\,\mathrm{cm^2\,sr^{-1}}$ using a value of $2.9 \times 10^{-30}\,\mathrm{cm^2\,sr^{-1}}$ for the Q-branch of nitrogen) by comparing lidar measurements with radiosonde measurements.[28] Using a similar technique, Melfi calculated this ratio as $3.8 \pm 25\%$ ($1.1 \times 10^{-29}\,\mathrm{cm^2\,sr^{-1}}$).[29] Strauch *et al*. using a comparison of lidar measurements with those from a microwave refractometer mounted at a height of 30.5 m on a tower obtained a cross-section ratio of approximately 3 ($8.7 \times 10^{-29}\,\mathrm{cm^2\,sr^{-1}}$).[30] The current best value for this ratio is $2.5 \pm 10\%$.[27] It is clear that more work needs to be done to determine this important parameter. We shall mention later a new effort that we hope will establish a significantly improved value for the ratio of water vapor and nitrogen cross-sections.

There was a relative lack of interest in Raman water vapor lidar following this early flurry of interest, presumably owing to increased interest in the DIAL approach to water vapor measurements because of the far larger signal strengths offered by the DIAL technique. However, with advances in the technology of lasers, detectors, and data acquisition systems, interest was renewed in Raman lidar later in the 1970s. Technological advances permitted the evolution of water vapor in the boundary layer to be quantified for the first time in 1977 using Raman lidar.[31] The same group produced the first daytime Raman lidar measurements of water vapor using a frequency-quadrupled neodymium-doped yttrium aluminum garnet (Nd : YAG) laser emitting at 266.6 nm.[32] At the wavelengths required for these measurements, sunlight is greatly attenuated by the stratospheric ozone layer. Hence, this portion of the spectrum is referred to as the solar blind region and is characterized by greatly reduced solar background levels. These reduced backgrounds allow for signals to be received with little or no additional background signal due to solar radiation. There are complications, however, in that atmospheric absorption due to ozone and possibly molecular oxygen, depending on the wavelengths used, must be accounted for.

Using a frequency-tripled Nd : YAG laser, measurements of the evolution of the water vapor field to greater altitudes and over longer time were demonstrated in the mid-1980s.[33] The state of the art of Raman lidar technology has now advanced to a point that permits automated Raman lidar measurements to be made during both the daytime and nighttime.[34] We shall discuss the details of this automated system and provide some examples of the data produced from this instrument later.

2.7 Water temperature

The Raman spectrum from liquid water is temperature sensitive, with the Raman scattered intensity covering a relatively large band ($2800-3800\,\mathrm{cm^{-1}}$).[35] Oceanic researchers have used this effect to measure subsurface water temperature from lidar, as first demonstrated in the mid-1970s.[36] This group operated a downward-looking Raman lidar from a ship using a spectrally filtered nitrogen laser. The filtered output insured that spontaneous emission in the laser was not interpreted as a signal from the water. The return signal was spectrally separated using a double spectrometer, allowing them to determine the water temperature at a depth of 1 m with an accuracy of $\pm 2\,^{\circ}\mathrm{C}$. Although there has been a relative lack of work in this field since then, recent efforts indicate renewed interest.[37,38]

2.8 Cloud liquid water

The remote detection of Raman scattering from liquid water in clouds was studied by Pourney *et al*. as a possible contamination of their water vapor measurements in the boundary layer.[31] They concluded that this influence should be negligible. Vaughan *et al*. also studied the possibility of Raman scattering contaminating the measurement of water vapor using the OH stretch region of $3657\,\mathrm{cm^{-1}}$.[39] Their conclusion was the same as that of Pourney *et al*. that the influence of any liquid scattering in the vapor band should be negligible. Bukin, however, demonstrated that the intensity of Raman scattering from cloud liquid was sufficient for remote measurements, although the measurements were not range resolved.[40] The first range resolved measurements of Raman scattering from liquid water in clouds was reported by Melfi *et al*., where the Raman scattering from liquid water was observed to produce a large enhancement of the water vapor signal due to the broad filters used in that study.[41] Whiteman and Melfi developed a retrieval technique based on these cloud measurements that permits the cloud liquid water, cloud droplet average radius, and number density to be derived.[35]

2.9 Atmospheric temperature

The first temperature measurements made using Raman lidar were performed in early 1971 by Strauch *et al*. using the vibrational nitrogen signal.[30] They remotely monitored temperature fluctuations at the top of a 30-m tower by establishing a correlation between the Raman backscatter and co-located temperature measurements using thermistors mounted on the tower. This same technique was later used by Keckhut *et al*.[42] to extend the measurement of

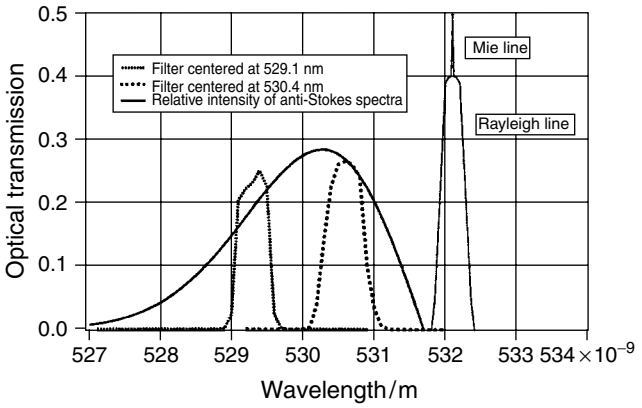

Figure 3. Position of the filters in the rotational Raman anti-Stokes spectrum to make temperature measurements, together with the transfer function of both filters used by Nedeljkovic *et al.*[46] [Reproduced from D. Nedeljkovic, A. Hauchecorne and M.-L. Chanin, *IEEE Trans. Geosci. Remote. Sens.*, **31**, 90 (1993) by permission of IEEE (© 1993 IEEE).]

stratospheric temperature to regions below 30 km where the method based on Rayleigh scattering[43] produced errors due to aerosol scattering.

Cooney proposed a completely different method of remote temperature determination using the temperature sensitivity of rotational Raman scattering from diatomic molecules such as N_2 and O_2.[28] The strengths of the rotational Raman lines of N_2 and O_2 vary according to the Maxwell–Boltzmann distribution. As temperature increases, increasingly higher quantum number transitions become more probable, causing changes in the relative distribution of line strengths in the profile. By positioning filters at two separated locations in the anti-Stokes spectrum (to avoid possible interference due to fluorescence) as in Figure 3, a temperature measurement is possible. Salzman and Coney first used this technique successfully in 1973 over a horizontal path of approximately 100 m.[44] It has since been used to probe the atmosphere throughout the troposphere and into the stratosphere.[45–48]

2.10 Extinction/optical depth

A direct measurement of the extinction due to tropospheric aerosols or cirrus clouds is possible with either a high spectral resolution lidar (HSRL)[49,50] or a Raman lidar.[51,52] In the case of the HSRL, the particle and molecular returns are separated using high-resolution filtering techniques. In the Raman lidar measurement of extinction, the attenuation of the vibrationally shifted return from either nitrogen or oxygen is measured and compared with a molecular density profile. In the absence of any attenuation other than that due to molecules, the Raman lidar signal will be proportional to the atmospheric number density once the range-squared and atmospheric transmission terms in the lidar equation are accounted for. Any deviations from this indicate the presence of additional aerosol attenuation. This has proven to be a very useful technique for understanding scattering and extinction properties of cirrus clouds[53] and tropospheric aerosols.[54]

2.11 Stratospheric ozone

A novel use of the Raman lidar technique has been in DIAL measurements of stratospheric ozone in the presence of atmospheric aerosols. Aerosols enhance the backscatter signal, which complicates the analysis of data acquired with an elastic DIAL. The Raman DIAL technique was first used by McGee *et al.* as a means to measure stratospheric ozone in the presence of volcanic aerosols due to the eruption of Mt Pinatubo in 1991.[55] The traditional elastic DIAL technique produced large errors below 30 km due to the additional scattering and attenuation by volcanic aerosols. Using the new technique, based on measuring Raman scattering from molecular nitrogen induced by two laser sources (308 nm XeCl excimer and 351 nm XeF excimer), McGee *et al.* were able to measure ozone in the crucial region below 30 km where the ozone peak typically occurs. Raman channels are now routine in stratospheric ozone lidar systems. A similar approach is also being used to account for ozone attenuation in the lower troposphere in solar blind water vapor measurements with Raman lidars.[56]

3 THEORY OF RAMAN LIDAR WATER VAPOR AND AEROSOL MEASUREMENTS

Most atmospheric lidar systems operate by transmitting a laser pulse into the atmosphere and recording the backscattered light as a function of time. Since normal Raman scattering is nonresonant, the wavelength of the outgoing laser beam is arbitrary (although shorter wavelengths are preferred owing to the larger Raman cross-sections), and the choice of the wavelength transmitted can be made to optimize the system in other ways. Using the Stokes component of Raman scattering, the energy shifts, which are unique for different molecular species, associated with water vapor and nitrogen are 3657 and 2329 cm^{-1}, respectively. These relatively large energy shifts allow the use of dichroic mirrors to separate the wavelengths into separate channels for detection.

The signal for each of these channels is described by the lidar equation,[57] given in equation (1):

$$S_i(r) = k_i r^{-2} O_i(r) \sigma_i(\pi) n_i(r) q(\lambda_0, r) q(\lambda_i, r) \qquad (1)$$

where S_i is the received signal in channel i as a function of range r, O_i is the optical overlap function describing the detector's field of view, $\sigma_i(\pi)$ is the 180° Raman backscatter cross-section for the species detected in channel i, n_i is the number density of that species, $q(\lambda_0, r)$ describes the transmission of the outgoing laser beam, and $q(\lambda_i, r)$ is the transmission of the backscattered signal. The Raman cross-section $\sigma_i(\pi)$ does have a temperature dependence, hence there is some dependence on altitude. However, at atmospheric temperatures (roughly 200–320 K) and using reasonably wide bandpass filters, these cross-sections are relatively constant[58] and are therefore often incorporated into the constant k_i. The constant k_i includes the laser pulse energy, the receiver's area, and the overall sensitivity of the channel.

The basic theory of Raman lidar measurements of water vapor is straightforward, and is illustrated in Figure 4. The water vapor mixing ratio is defined as the mass of water vapor divided by the mass of dry air in any given parcel of air. Nitrogen is well mixed in the troposphere, hence the ratio of the mass of water vapor to the mass of nitrogen is proportional to the actual water vapor mixing ratio at a given altitude. The Raman scattered intensity is a function of the number of molecules of the species of interest as shown in equation (1). Because of this, the water vapor mixing ratio is derived from a Raman lidar by taking the ratio of the return at the wavelength associated with water vapor Raman scattering and the return associated with nitrogen Raman scattering. Two corrections must be applied: one to account for the mismatch of the laser and detector's field-of-view (FOV) (called the overlap correction), and another to account for differential transmission due to the wavelength dependence of Rayleigh and aerosol scattering. Owing to the uncertainty in the water vapor cross-section, a final height-independent calibration factor, which is typically derived from another measurement of water vapor, is then applied to convert this ratio of signals into a mixing ratio. Further details of the calculation of water vapor mixing ratio can be found elsewhere.[34,59,60]

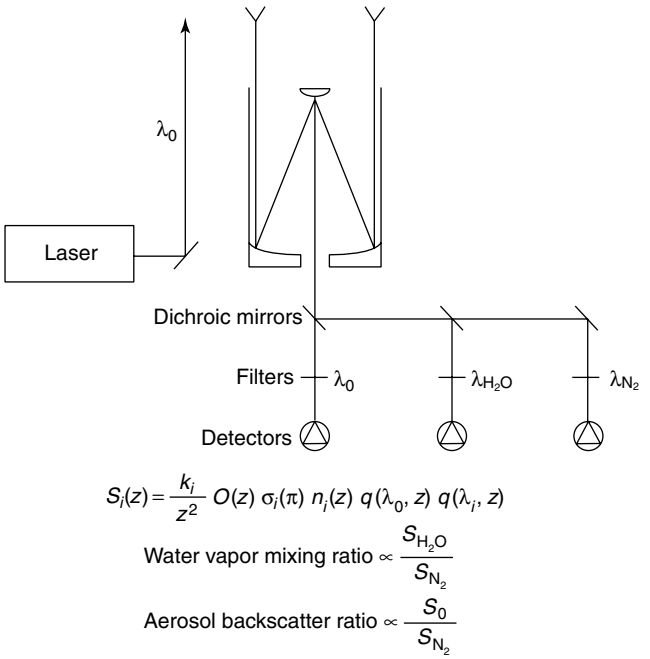

Figure 4. Basic Raman lidar concept. [Reproduced by permission of the Optical Society of America from J.E.M. Goldsmith, F.H. Blair, S.E. Bisson and D.D. Turner, *Appl. Opt.*, **37**, 4979 (1998).]

After deriving the water vapor mixing ratio, atmospheric profiles of relative humidity can be calculated if the ambient temperature profile is known. Temperature profiles can be derived from Raman lidar measurements as described above, or can be measured by other sensors such as radiosondes, models, or retrievals from radiance measurements.[4] The mixing ratio profile can also be integrated as a function of altitude to retrieve total precipitable water vapor (PWV) in the column.

The derivation of the aerosol scattering ratio, which is defined as the ratio of molecular + aerosol scattering to molecular scattering, is very similar to the water vapor mixing ratio calculation. To derive this quantity, the elastic return, i.e. the return at the laser wavelength which is composed of Rayleigh and Mie backscatter events, is divided by the Raman return associated with nitrogen, which is a purely molecular event. Like the water vapor mixing ratio calculation, corrections are made to account for the overlap and the differential transmission. The ratio is then normalized to unity in an altitude region where there is assumed to be negligible aerosol scattering. More details on the calculation of aerosol scattering ratio are given elsewhere.[54,60,61]

After calculating the aerosol scattering ratio, profiles of aerosol backscatter coefficient, which is the backscatter at 180° (or directly back to the receiver), can be calculated. A temperature profile is required to compute the molecular number density, from which the molecular backscatter coefficient can be calculated. Knowing the molecular backscatter coefficient allows the aerosol backscatter coefficient to be determined from the aerosol scattering ratio. Ferrare *et al.*[54] demonstrated this calculation in more detail.

As indicated earlier, only two types of lidars are able to derive aerosol extinction coefficients independently of the aerosol backscatter: high spectral resolution and Raman lidars. In both of these types of lidars, a purely molecular signal is measured, and the total extinction along the path is related to the slope of the lidar signal.[62] Again, an ambient temperature profile is required to calculate the extinction due to molecules, which is subtracted from the total extinction profile to yield the aerosol extinction coefficient profile. The method to calculate aerosol extinction from Raman

lidars was first demonstrated by Ansmann *et al*.[51] In Raman lidars, the backscatter profile typically used for extinction measurements is either a profile of nitrogen or oxygen Raman backscatter, both of which are well mixed in the troposphere and lower stratosphere. This same technique can be used to derive extinction in clouds[53] as long as multiple scattering is accounted for.[63,64]

4 ARM CART RAMAN LIDAR

The US Department of Energy's largest climate research program, the Atmospheric Radiation Measurement (ARM) program, was designed to address the need for extended measurements of water vapor, clouds, aerosols, and other constituents in the atmosphere that influence or control the transmission of radiant energy through the atmosphere. This knowledge is imperative to understanding and improving climate models, as the treatment of the radiative transfer was one of the largest uncertainties in these models.[65,66] To make continuous measurements of the various atmospheric geophysical parameters needed, such as water vapor, with high accuracy for long time periods (up to 10 years or longer), the program turned to developing various remote sensors. Many of these remote sensors were strictly laboratory instruments or perhaps prototypes, and thus the program worked to evolve them into instruments capable of operating autonomously. Raman lidar had proven to be a valuable tool for making water vapor and aerosol measurements during campaigns.[33,52] Owing to the simplicity of the technique and minimal constraints that are placed upon the laser, it was considered a more probable candidate to automate than a DIAL for the water vapor measurements that are critical to the success of ARM. As such, a Raman lidar, designed and built specifically for the ARM program, was developed to make measurements of water vapor, aerosols, and clouds throughout the diurnal cycle with a minimum amount of user intervention. This system is deployed at the ARM Cloud and Radiation Testbed (CART) site in north-central Oklahoma, USA.

Since Raman scattering is a relatively weak scattering process, the detection of the Raman signal during the daytime in the presence of a high solar background is much more difficult than at night. There are two general approaches for making daytime Raman lidar measurements: to operate in the solar blind regime of the spectrum (i.e. at wavelengths less than approximately 300 nm) or to use narrow-band, narrow-FOV operation. Model results indicate that both techniques offer approximately the same level of daytime performance.[67] However, operation in the solar blind has a much more limited range at night owing to the absorption by ozone (which makes the daytime solar blind measurements possible) than the narrow-band, narrow-FOV approach. Therefore, the ARM CART Raman lidar (CARL) is based on the narrow-band, narrow-FOV approach. A second wider FOV was also incorporated in order to improve short-range measurements and to extend the dynamic range of the system. Renaut and Capitini[68] and Balsinger and Philbrick[56] presented some examples of Raman lidar systems operating in the solar blind, whereas Bisson *et al*.[69] and Wessel *et al*.[70] gave examples of other narrow-band, narrow-FOV Raman water vapor lidars.

The CARL was designed to operate unattended in the variable, and sometimes hostile, Oklahoma environment. It is enclosed in an approximately 6.1 m long by 2.4 m wide by 2.4 m high metal shipping container. This container houses the laser, all of the optics, the computer and data acquisition system, and the environmental controls. The only requirement is an external supply of conditioned 208-V, three-phase power, which is provided through a large uninterruptible power supply (UPS), as there are frequent power interruptions at the rural site. The temperature in the container is maintained within approximately 2 °C to minimize any changes in the system due to temperature fluctuations. High-efficiency particulate air filters were incorporated into the environmental control system to maintain the cleanliness of the system. A computer rack houses the data acquisition hardware and controlling personal computer, and data are routinely transferred to the ARM data system for further processing which yields the geophysical parameters of interest such as water vapor and aerosol profiles.

All of the optical components are mounted on a single, rigid optical bench to reduce the influence of any vibrations. The 61-cm telescope is oriented vertically beneath a weather-tight high-quality optical window. To protect the system further against hail, a shield made of stainless-steel mesh was constructed and placed above the window. This hail shield has an opening above the thicker laser-transmitting window, which is inset in the center of the main window, so that the outgoing laser beam is not affected by the laser shield. Finally, a baffle was placed around the window to shield the telescope from direct sunlight. A schematic diagram of the system enclosure and overall layout is given in Figure 5.

The CARL uses a frequency-tripled Nd : YAG laser, operating at 30 Hz with 300–400-mJ pulses to transmit light into the atmosphere at 355 nm. Automated routines periodically adjust the second- and third-harmonic generator crystals to maintain maximum laser energy. As this is an autonomous system, eye safety is an important consideration, and to accomplish this the outgoing beam is expanded 15-fold (to approximately 13 cm in diameter). The expanded beam also helps to reduce the outgoing beam's divergence to less than 0.1 mrad, allowing for a small FOV to be used on the receiver.

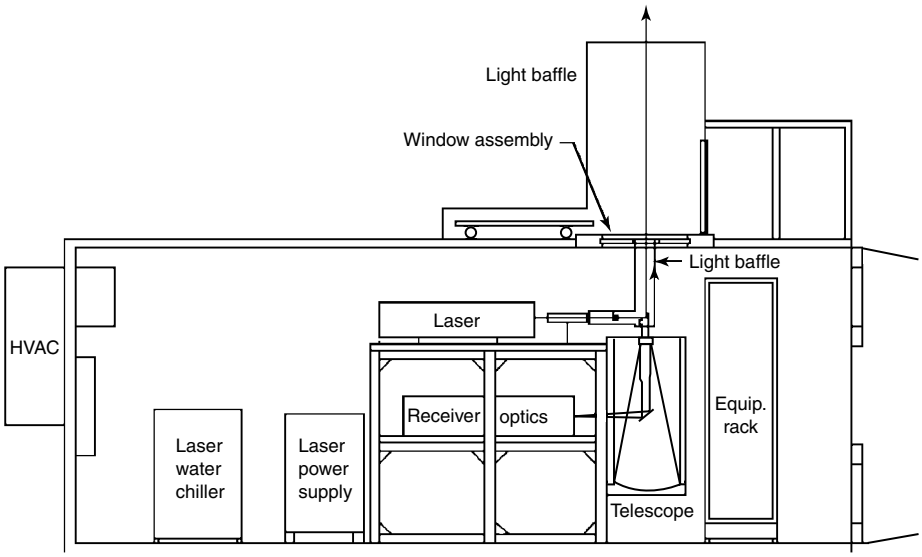

Figure 5. Layout of the CART Raman lidar system (side view). HVAC stands for heating, ventilation, and air conditioning. [Reproduced by permission of the Optical Society of America from J.E.M. Goldsmith, F.H. Blair, S.E. Bisson and D.D. Turner, *Appl. Opt.*, **37**, 4979 (1998).]

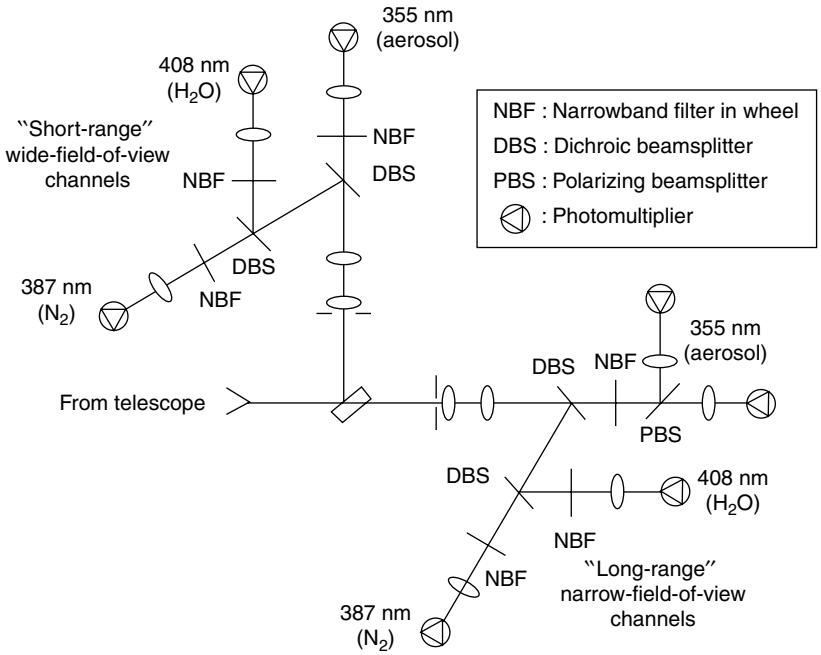

Figure 6. Optical layout of the aft detection optics of the CART Raman lidar receiver. [Reproduced by permission of the Optical Society of America from J.E.M. Goldsmith, F.H. Blair, S.E. Bisson and D.D. Turner, *Appl. Opt.*, **37**, 4979 (1998).]

The receiver optics of this lidar are shown in detail in Figure 6. Incoming light from the telescope is split into the two fields of view by a wedged beamsplitter. After this point, the detection systems for the narrow and wide FOVs are entirely independent. The wide FOV is 2 mrad and the narrow FOV is 0.3 mrad. After the field stops (which set the FOVs), the light is separated by dichroic mirrors and narrow-band interference filters [full width at half-maximum (FWHM) intensity of 0.4 nm] into several channels. All of the channels use photon counting, and the temporal resolution of the bins is 260 ns, which corresponds to 39 m vertical resolution. Data are typically summed for approximately 1740 laser shots (1 min) before transferring data to the collection computer. These channels measure the elastic Rayleigh–Mie backscatter at the laser wavelength (355 nm), the Raman backscatter due to water vapor (408 nm), and the Raman backscatter due to nitrogen (387 nm) simultaneously. Owing to the high solar

background and the count rate limitation of the current data acquisition electronics, the narrow FOV water vapor measurements made during the daytime are acquired with a 10% transmission filter installed. The elastic return in the narrow FOV channel at the laser wavelength is separated into its parallel and perpendicular components (with respect to the polarization of the laser beam), from which one can compute the linear depolarization ratio of the backscatter.

Although Raman lidars can be absolutely calibrated in principle, the uncertainty in the ratio of the water vapor to nitrogen Raman cross-sections (which is of the order of 10%) is the limiting factor. Therefore, Raman lidars are typically calibrated by deriving a height-independent calibration factor for the Raman lidar data from another independent instrument that measures water vapor. Historically, radiosondes have been used for this purpose.[71] However, further research has shown that a dry bias exists in the type of radiosonde used by many field programs, including those launched by the ARM program.[72,73] The cause of this dry bias has been determined,[74] but the correction only improves the mean agreement and does not work to reduce the sonde-to-sonde variability that was discussed by Turner *et al*.[72] Clough *et al*. argued that measurements of the 22-GHz water vapor absorption line, which are made routinely at the ARM CART site by a passive microwave radiometer (MWR), can serve as an absolute reference for water vapor calibration.[75] Therefore, the CARL is calibrated to agree in PWV measurements retrieved by the MWR,[59,76] which retrieves PWV from measurements of the zenith brightness temperature at this frequency.[77]

One measure of the operational status of an instrument is the fraction of time during which the system is collecting data. Figure 7 shows the percentage of time the CARL was operational per month for a recent 25-month window. The main source of downtime between April 1998 and February 1999 was frequent momentary interruptions in power at the rural CART site, which caused the laser to stop. A UPS was installed in February 1999 to condition the power for the lidar. Solving this problem revealed another problem in the software of the system, which was solved when the computer was upgraded in September 1999. Problems with the laser periodically punctuated mid-to-late 1999, which required service from the laser vendor. However, October and December 1999 and March–April 2000 showed system uptimes of over 95%, a feat currently unachieved by any other autonomous water vapor lidar system. This period translates into over 9000 h of data collected, or over 54 000 10-min profiles. During this same period, the CART site released only 2354 radiosondes from its co-located launch site. The Raman lidar data therefore provide much higher temporal resolution for studying changes in atmospheric water vapor than the radiosondes used at the CART site.

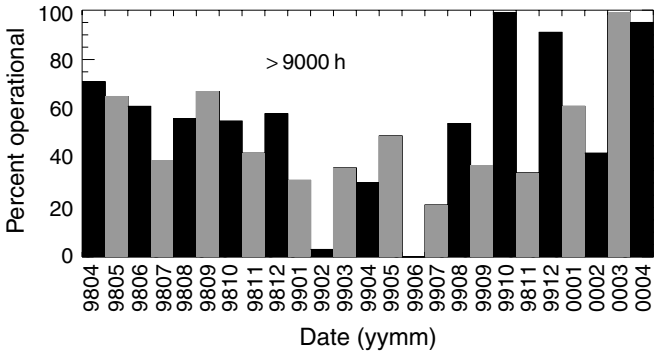

Figure 7. The percentage of time the CART Raman lidar has been operational per month for a 25-month period. Over 9000 h of data were collected during this period.

To specify fully the atmospheric state above the CART site, profiles of temperature and wind are needed. Whereas temperature profiles can be retrieved from a Raman lidar,[47,48,78] the CARL has not been configured to measure temperature. Instead, we use temperature profiles physically retrieved from the Atmospheric Emitted Radiance Interferometer (AERI), which is located within 150 m of the lidar. Details of the AERI's temperature retrieval are given elsewhere.[4,79] These temperature data are used to compute relative humidity from the Raman lidar, and also to calculate molecular number density for the aerosol retrievals. The water vapor and aerosol data from the lidar, temperature data retrieved from the AERI, and wind data from the 915-MHz radar wind profiler (also at the CART site) allow the state of the atmosphere to be fully specified by remote sensors in noncloudy situations.[76] In the next section, we highlight a variety of ways in which these remote sensing data, and in particular the Raman lidar, are being used to gain insight into atmospheric processes by ARM and the general scientific communities.

5 EXAMPLES

5.1 Example profiles

Before we discuss the various ways to utilize the Raman lidar data, some example water vapor and aerosol profiles retrieved from CARL will be presented. In Figures 8–10, the error bars indicate the random errors that are calculated assuming Poisson statistics from the detected photon counts. Therefore, the random error will decrease by the square root of n, where n denotes the factor by which either the temporal or spatial summing of the data has been increased. For example, summing together two 10-min profiles will in general reduce the size of the error bars by approximately 40%. The temporal resolution for all data

shown in this paper is 10 min unless noted otherwise (1-min resolution is possible for many of these products), and the vertical resolution varies as a function of altitude for each quantity being derived.

Figure 8 shows comparisons of the lidar-observed water vapor mixing ratio profile and that measured by radiosondes. Figure 8(a) is a daytime measurement occurring at 14 : 33 local time (20 : 33 GMT) on 1 October 1999. The Raman lidar and radiosonde profiles are in good agreement below 4 km, above which the lidar's measurement becomes noisy owing to the large solar background. As indicated above, during the daytime the large solar background increases the count rate by several orders of magnitude in the narrow FOV water vapor (408-nm) channel. To ensure that the signal remains in a region where the detector responds in an approximately linear manner, 90% of the signal from this channel is thrown away in the daytime by the use of a 10% transmission filter. New detection electronics with a larger dynamic range are currently being investigated to see if this signal can be recovered. Note that the 10% transmission filter is automatically removed by the system at night, since the count rates in this channel decrease as the solar background decreases.

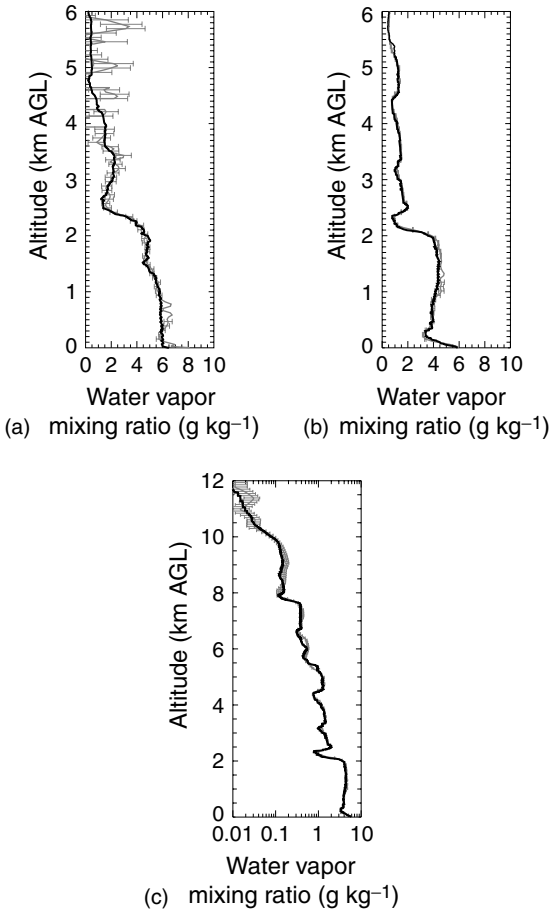

Figure 8. Example of water vapor mixing ratio profiles observed by the CART Raman lidar (gray with error bars) and coincident radiosondes (black) during the daytime [(a), 14 : 33 local time], and at night [(b) and (c), 5 : 30 local time] on 1 October 1999. Note the logarithmic abscissa and the extended height range in (c) emphasizes the performance of the two observational systems in the upper troposphere.

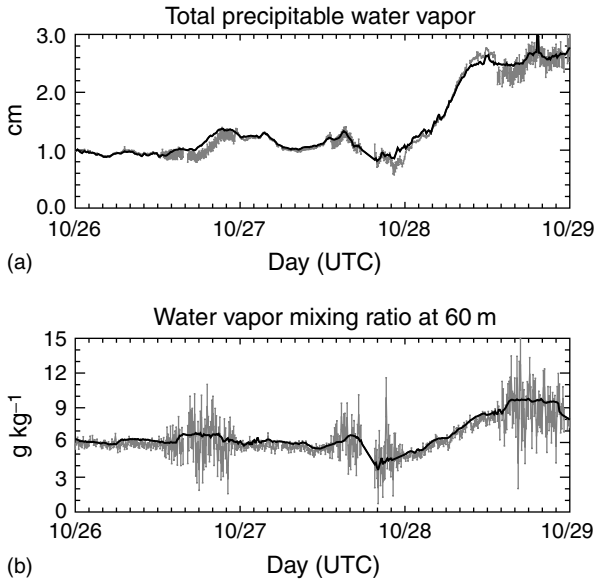

Figure 9. Coincident total PWV data observed by the Raman lidar (gray with error bars) and the MWR (black) for a 3-day period in October 1999 (a), and observations of water vapor mixing ratio from the Raman lidar's first bin (gray with error bars) and the in situ probes on the 60-m tower (b). Note that sunrise is approximately 1200 UTC (universal time coordinates), which corresponds to the increase in the random error in the Raman lidar measurements.

There is some disagreement between the lidar and radiosonde between 600 and 900 m where the two FOVs are merged together during the daytime. This is due to the large random error in the wide-FOV channel, which admits a much larger fraction of solar background than the narrow-FOV channel. It should be noted that the merge region is a compromise of various factors, which take into account the random error, overlap correction, and dead-time corrections. The vertical resolution of the lidar data is 78 m.

Figure 8(b) demonstrates a night-time comparison of water vapor mixing ratio profiles observed by the lidar and radiosonde. This measurement occurred at 5 : 30 local time (11 : 30 GMT) on 1 October 1999. Again, there is excellent agreement between the lidar and the radiosonde results, even though the lidar profiles vertically and the radiosonde drifts with the wind away from the site. Note the greatly reduced error in the lidar measurements compared with the daytime error values. Figure 8(c) shows the same night-time profiles plotted on a logarithmic abscissa to emphasize the low water vapor amounts in the upper troposphere. In this example, the two profiles are in good agreement

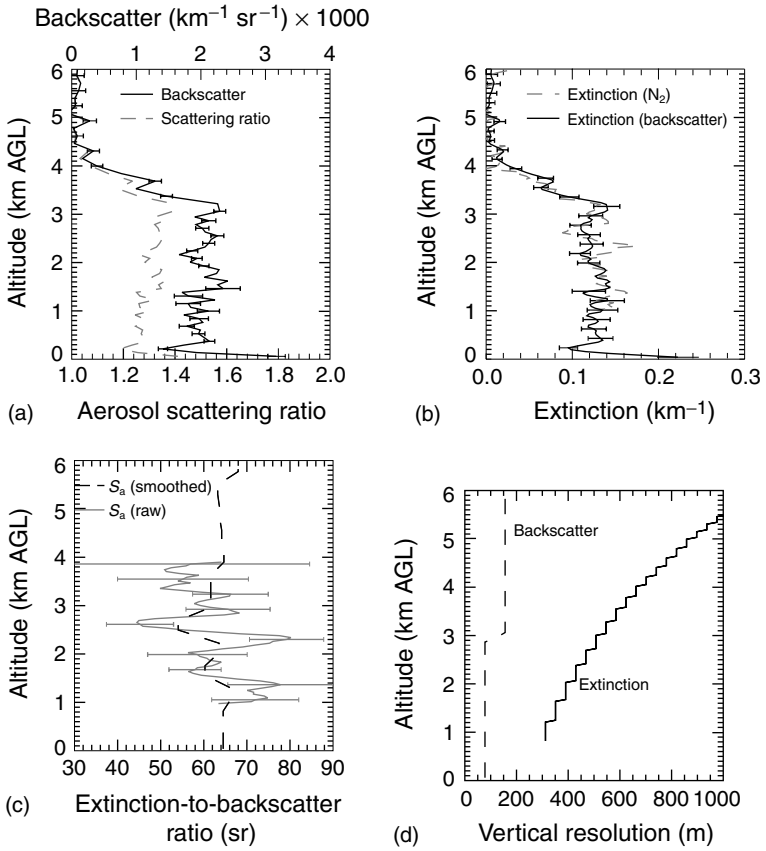

Figure 10. Aerosol profiles derived from the CART Raman lidar on 1 September 1998 at 0600 UTC. (a) Aerosol scattering ratio and backscatter profiles, with error bars included on the backscatter profiles. (b) Aerosol extinction profiles derived from nitrogen data only, and derived from aerosol backscatter using the smoothed extinction-to-backscatter ratio (S_a) profile. (c) The smoothed S_a profile, along with the raw S_a profile, is shown. The smoothing of the S_a profile is discussed elsewhere.[61] (d) The vertical resolution used for the backscatter and extinction measurements. These profiles are 10-min averages.

throughout the entire column. The vertical resolution of the lidar's data is 78 m up to 6 km, gradually decreasing to 312 m above 11 km.

The PWV is derived from the Raman lidar by integrating the water vapor mixing ratio profiles as a function of height, which can then be compared with the PWV retrieved by the MWR. A three-day time series of PWV from 26 to 29 October 1999 observed by each system is given in Figure 9(a). Note the very small random error in the Raman observations at night (0000–1200 UTC hours on each day). As indicated earlier, the CARL is calibrated to the MWR. A single height-independent calibration factor is determined from the night-time data on three consecutive nights centered upon the day of interest, and this factor is applied to all of the lidar data for the entire day. This process is repeated for each day. Turner *et al*. indicated that the calibration factor varies by ca 3–4% over an 8-month period.[76] Another factor hampers the comparison of PWV observed by the lidar and the MWR, however. As indicated above, the lidar is only able to profile to approximately 3.5 km during the daytime and maintain a relatively low random error. The strength of the Raman water vapor return, and hence the maximum altitude that can be profiled, vary depending on a variety of conditions, which include output laser energy, water vapor amount, and other factors.[71] Typically, the CARL is able to sense about 70–85% of the total amount of water vapor in the column during the daytime owing to the restricted height. In order to compute PWV during the day, the fraction of the water vapor that the lidar senses has to be determined and can then be scaled up to account for this,[59] but this introduces some additional error that is hard to estimate.

The first range gate of the lidar is at 60 m, and so comparisons between the lidar and the in situ probe on the 60-m tower (located about 125 m west of the lidar) can be performed. This comparison is shown in Figure 9(b) for the same three-day period. At this level, the signal-to-noise ratio is very small during the daytime owing to geometric considerations of the receiver and the high solar background, hence the daytime measurements are fairly noisy. However, the low random error at night

allows this system to be calibrated to the in situ probes, which are absolutely calibrated in a salt-bath solution, and offer a calibration alternative to the MWR. Calibrating CARL to agree with the 60-m tower is very sensitive to small errors in the overlap correction at 60 m; however, the two calibration techniques typically agree to better than 5%.

Examples of the aerosol products derived from the Raman lidar are given in Figure 10. These data show a relatively uniform aerosol layer extending from the surface to about 3.5 km. The vertical resolution of the backscatter coefficient (and aerosol scattering ratio) and the extinction coefficients is given in Figure 10(d). By decreasing the vertical resolution of the extinction profile, a relatively constant random error level is maintained at all altitudes.

5.2 Evolution of the water vapor field

One of the strengths of Raman lidar is the high spatial and temporal resolution of its measurements. The development of a Raman lidar to profile water vapor throughout the diurnal cycle autonomously has provided a unique dataset to study the evolution of water vapor in the lowest layers of the atmosphere. Figure 11 shows a 28-day time–height cross-section of water vapor mixing ratio over the SGP site

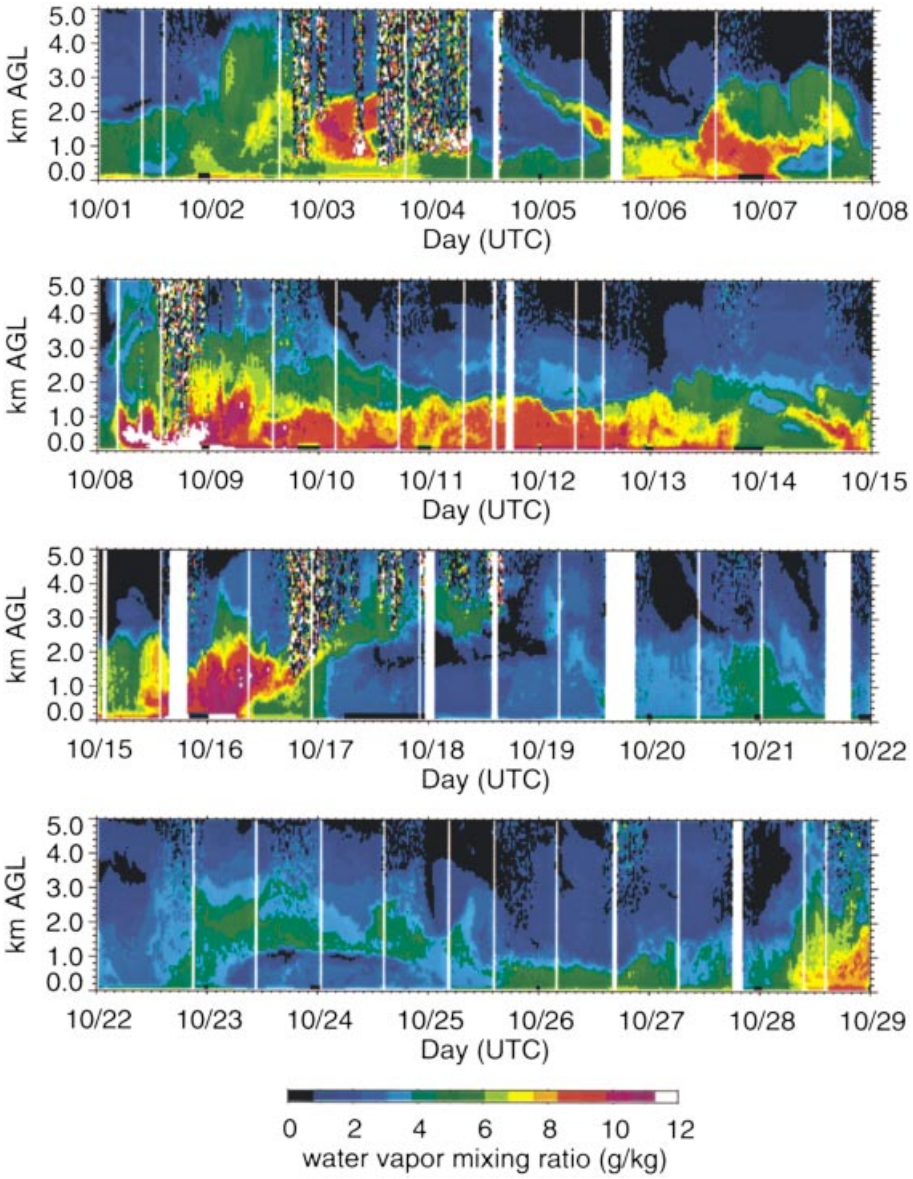

Figure 11. A 28-day time–height cross-section of water vapor mixing ratio for 1–28 October 1999 at the SGP CART site. The vertical white bars indicate periods where the lidar was offline or was collecting calibration data sets. Note the large variability in the water vapor field, in both time and height.

from 1 to 28 October 1999. This image demonstrates many intriguing features, including the entrainment of a moisture plume into the boundary layer on 5 October, precipitation events (3 and 4 October), cold front passages on 7 and 16 October, and the remarkable variability of the water vapor field in general. Melfi and Whiteman[33] were the first to use Raman lidars to study the evolution of the boundary layer for extended periods of time (although their studies were conducted only at night). Linné *et al.*[8] showed that CARL can be used to study turbulent transport in the boundary layer at night, but the random error during the daytime (which approaches 15%) is too large for boundary layer turbulence studies. The use of analog electronics in the CARL data acquisition could potentially eliminate the need for the 10% transmission filter in the daytime high-channel water vapor measurement. This would greatly improve the usefulness of the CARL data for this type of study. Another phenomenon that is being investigated with Raman lidar data is the occurrence of the nocturnal low-level jet that develops over the Southern Great Plains primarily during the spring.[80] Other Raman lidars[81] have been used to study the water vapor in the boundary layer with great detail.

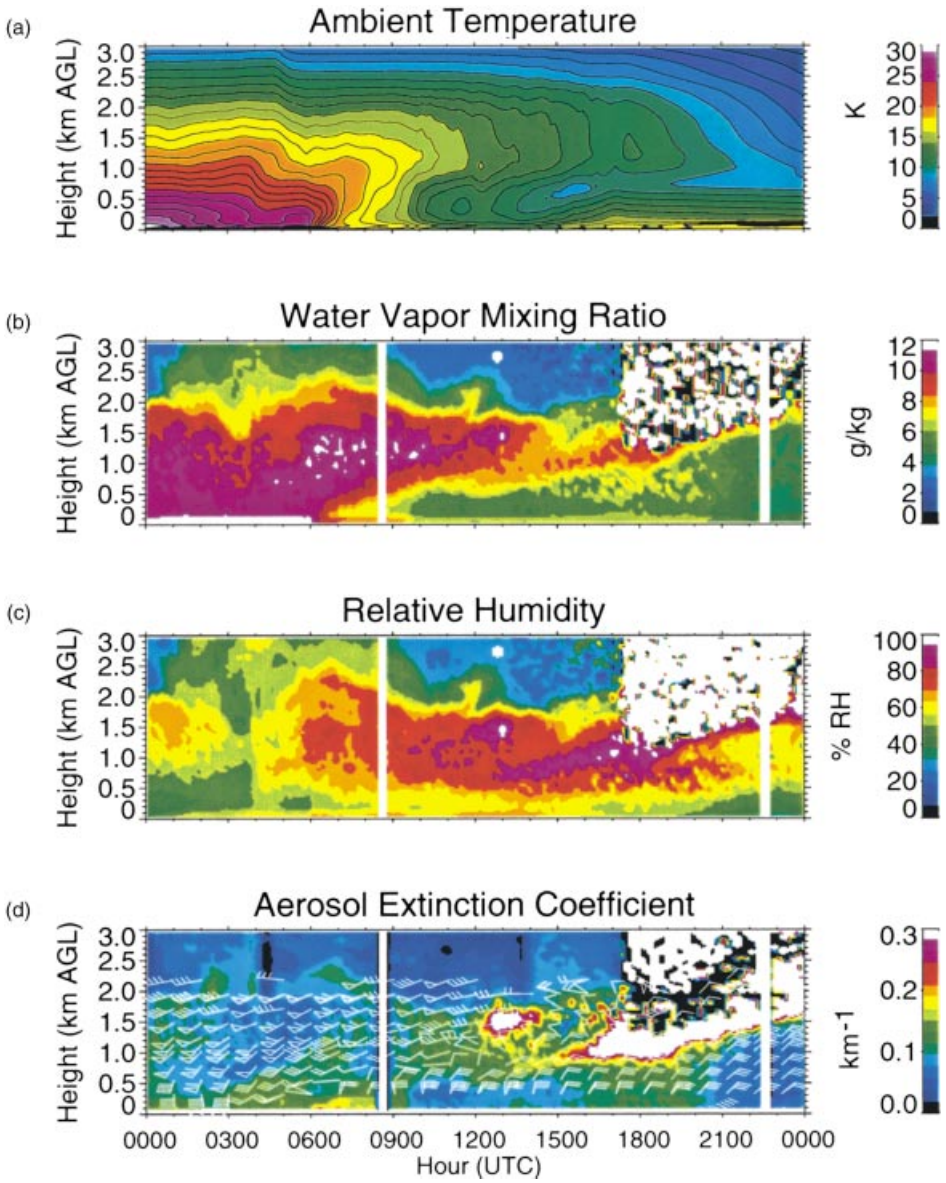

Figure 12. Time–height cross-sections of ambient temperature derived from the AERI (a), water vapor mixing ratio observed by the Raman lidar (b), relative humidity derived using AERI temperature and Raman lidar mixing ratio data (c), and aerosol extinction derived from the Raman lidar (d) for a cold-frontal passage on 16 October 1999. Wind data from a co-located 915-MHz radar wind profiler are overplotted on the aerosol data. The Raman lidar and AERI data are at 10-min resolution and, the wind profiler data are hourly averages. The surface cold frontal passage is evident in the temperature and mixing ratio images at 0700 UTC. See text for details.

5.3 Observation of atmospheric boundaries

Atmospheric fronts are the transition zones between two air masses of different densities. These two air masses typically have different temperatures and often also have different moisture contents. The high temporal and spatial resolution of remote sensor data (Raman lidar, AERI retrieval, and wind profiler) allows these frontal boundaries to be studied in great detail. Figure 12 shows time–height cross-sections of the ambient temperature retrieved from the AERI (a), the water vapor mixing ratio from the Raman lidar (b), the relative humidity computed from the lidar's mixing ratio using the AERI's retrieved temperature (c), and the aerosol extinction coefficient derived from the Raman lidar (d) as a cold front passed over the CART site on 16 October 1999. The profiles of wind direction and speed measured by the 915-MHz radar wind profiler[82] are overlaid on the extinction cross-section. The boundary of this cold front passed over the site at 0700 UTC, and is clearly identified in the surface meteorological data (not shown), and also the temperature and mixing ratio images. At this time, the winds at the surface (as

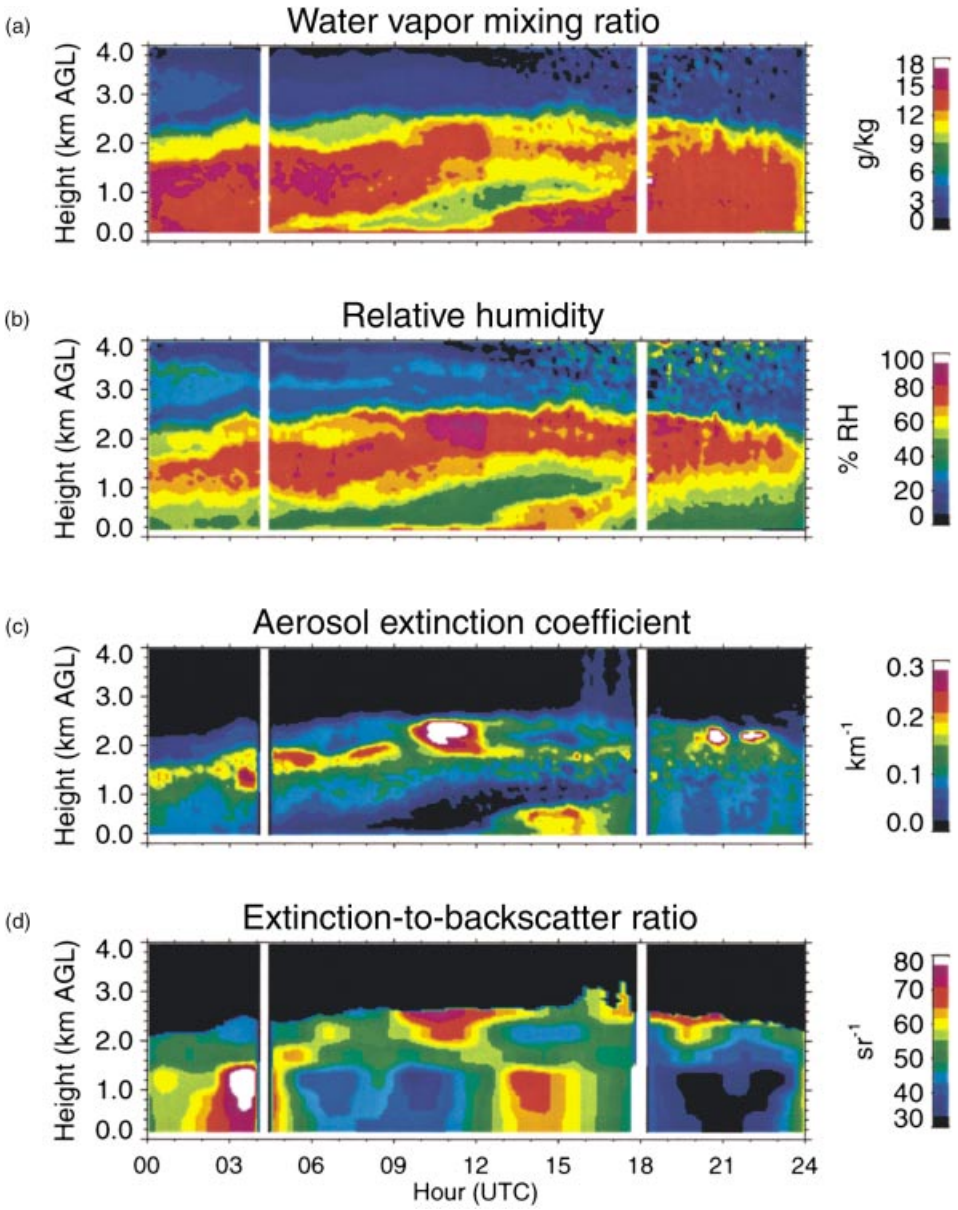

Figure 13. Time–height cross-sections of water vapor mixing ratio from the Raman lidar (a), relative humidity calculated using Raman lidar moisture and AERI temperature data (b), and aerosol extinction (c) and aerosol extinction-to-backscatter ratio (d) data for 28 August 1999. Periods where the mixing ratio is constant but the relative humidity and aerosol extinction is changing, which is the case at 2030 UTC, provide excellent opportunities to study the hydroscopic growth of aerosols in ambient conditions.

observed by a surface meteorological system, not shown) changed rapidly from west-south-west to northerly, and a gust front on the leading edge of the boundary picked up surface particulates (i.e. dust), which is clearly seen in the extinction image at 0600–0730 UTC. The wind profiler showed a large change in wind direction in the lowest 500 m, as the winds turned from southwesterly to northerly in the period of 1 h. The intrusion of cold air lifted the warmer, moister air, and eventually clouds formed along the boundary at 1700 UTC. Other examples of Raman lidar observations of frontal boundaries can be found elsewhere.[76,83,84]

5.4 Aerosol processes

The radiative impact of aerosols varies greatly as a function of the physical and chemical properties of the aerosols. These intrinsic properties, such as composition and size distribution, are related to extrinsic optical properties. Relative humidity has been shown to be the single most important parameter in determining the direct forcing due to aerosols.[85] The Raman lidar is able to measure aerosol extinction, backscatter, and hence the extinction-to-backscatter ratio (which is a function of the single scatter albedo and backscattering phase function) of the aerosols in their ambient environment. Since Raman lidars can measure the relative humidity and aerosols simultaneously, Raman lidars are a critical tool for understanding the relationship between relative humidity and the hydroscopic growth of aerosols in the atmosphere.

The first step in studying the hydroscopic growth of aerosols is to identify periods where the airmass is relatively unchanged, as changes in aerosol properties can be the result of changes in airmass. As indicated by Ferrare *et al.*,[54] the water vapor mixing ratio, which is conserved under all processes except evaporation and precipitation, is an excellent tracer of atmospheric motion, hence the identification of constant mixing ratio, especially if the mixing ratio is constant with altitude, suggests an unchanged airmass. Therefore, periods are identified where the water vapor mixing ratio is constant with altitude, which typically means that the relative humidity is increasing with altitude (because the temperature typically decreases with altitude). The time–height cross-sections of water vapor mixing ratio (a), relative humidity (b), aerosol extinction (c), and aerosol extinction-to-backscatter ratio (d) for 28 August 1999 are shown in Figure 13. At 2030 UTC (15 : 30 local time), the mixing in the boundary layer is at its peak, and the water vapor mixing ratio is relatively constant between 1 and 2 km, while the relative humidity is changing by more than 20%. Extracting these water vapor and the associated aerosol extinction and extinction-to-backscatter ratio

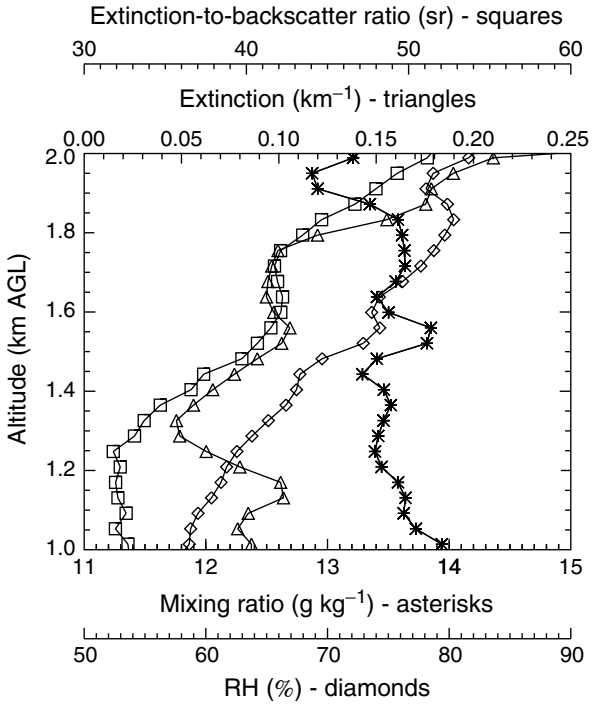

Figure 14. Profiles of water vapor mixing ratio, relative humidity λ (RH), aerosol extinction, and aerosol extinction-to-backscatter ratio for 28 August 1999 at 2030 UTC. Note the large increase in the aerosol extinction and extinction-to-backscatter profiles as the relative humidity increases.

profiles (Figure 14), these data show that the extinction value doubles through this layer, and that the extinction-to-backscatter ratio also becomes significantly larger as the relative humidity increases. The CARL has observed numerous cases such as these, which are being analyzed by the method of Ferrare *et al.*[54] to understand better the statistical relationships between relative humidity and aerosol properties. Other efforts have investigated this relationship using other types of lidars,[86] but have lacked the simultaneous measurements of aerosol extinction and relative humidity.

5.5 Aerosol and water vapor climatologies

The automation of the CART Raman lidar and its processing codes has resulted in over 9000 h of data being collected in an approximate 2-year span. These data were analyzed to produce mean profiles of water vapor and aerosol as a function of integrated amount [i.e. PWV or aerosol optical thickness (AOT)]. Figure 15 shows mean profiles of aerosol extinction, water vapor mixing ratio, and relative humidity acquired by the CART from April 1998 to January 2000. The mean extinction profiles are created as a function of AOT, where the distribution of AOT as a percentage of

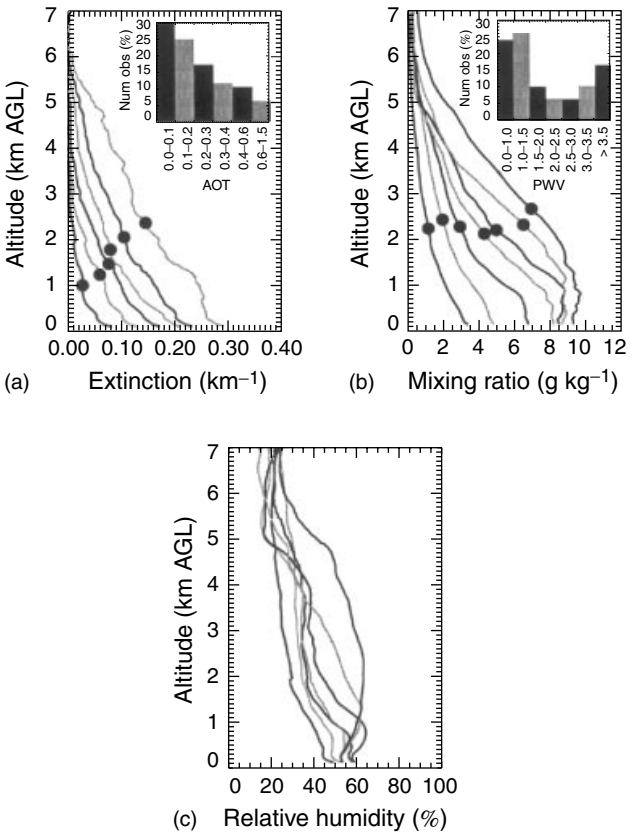

Figure 15. Mean aerosol and water vapor profiles for data from April 1998 to January 2000 as a function of AOT and PWV, respectively, for aerosol extinction (a), water vapor mixing ratio (b), and relative humidity (c). There is one mean profile per bin in the inset histograms, which indicate the distribution of the integrated amount over this approximately 2-year period, with profile (a) associated with the smallest bin, etc. [for the relative humidity profiles, the bins correspond to the profiles from (a) to (c) at 2 km]. The dots on the mean profiles indicate the scale height of these profiles. Note how the scale height increases from 1 to 2 km in the mean extinction profiles as the AOT increases, yet the scale height of the water vapor mixing ratio profiles remains relatively constant.

all observations, is given in the inset plot in Figure 15(a). The mean water vapor mixing ratio and relative humidity profiles are shown in Figure 15(b) and (c), respectively, separated as a function of PWV. The distribution of PWV for this period is given in the inset plot in Figure 15(b). The solid dots on the mean extinction and water vapor mixing ratio profiles indicate the scale height of these profiles, i.e. the point where 1/e of the integrated amount is above the point. Note how the scale height of the mean extinction profiles increases in altitude as a function of integrated amount, whereas the scale height of the mixing ratio profile is relatively constant. This indicates that the two geophysical parameters do not scale in the same way. A more detailed climatology of the water vapor and aerosols over the CART site, as measured by the Raman lidar, was given by Turner *et al.*[61]

5.6 Upper tropospheric humidity

Upper tropospheric (i.e. above approximately 7 km) humidity measurements are difficult to make owing to the very low amounts of water vapor and the very cold conditions that exist at those altitudes. However, this regime is very important climatically, as errors in the water vapor measurements at these altitudes cause disproportionately large errors in calculating the net radiation escaping to space.[87] Raman lidars are able to profile water vapor to near the tropopause during the night, and have been compared with other measurements of upper tropospheric humidity.[59,88] Figure 16 shows the mean difference of 74 comparisons of water vapor profiles between the CARL and radiosondes during two field programs that occurred in the fall of 1996 and 1997. The differences in water vapor mixing ratio (a) and relative humidity (b) are expressed as a percentage. Note the large difference in mixing ratio above 7 km, where the radiosonde becomes dry relative to the Raman lidar. Using these 74 cases, the outgoing longwave radiation (OLR) was calculated using a rapid radiative transfer model.[89] The mean difference in OLR between the lidar-driven calculations and the radiosonde-driven calculations is approximately 25% of the signature one would expect from a doubling of carbon dioxide. Therefore, errors in measuring water vapor in the upper troposphere can disguise the impact of increasing carbon dioxide in the atmosphere. From these data, we are unable to determine which measurement technique, the Raman lidar or the radiosonde, is more accurate,[90] hence upper tropospheric moisture remains a critical issue.

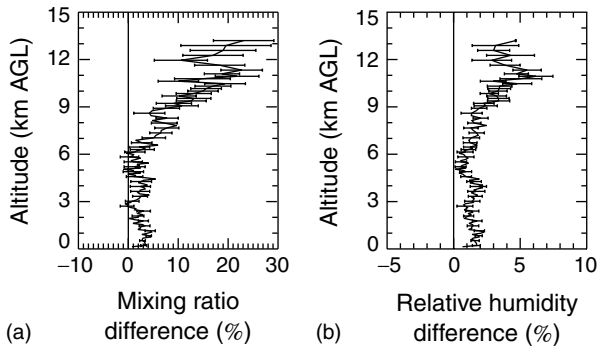

Figure 16. Mean difference of 74 coincident samples from September 1996 and September 1997 between night-time CART Raman lidar data and radiosondes. At altitudes above 7 km, the radiosonde becomes increasingly drier with respect to the Raman lidar, and uncertainties of this magnitude, when introduced into models, are effectively 25% of the signal associated with the doubling of carbon dioxide.

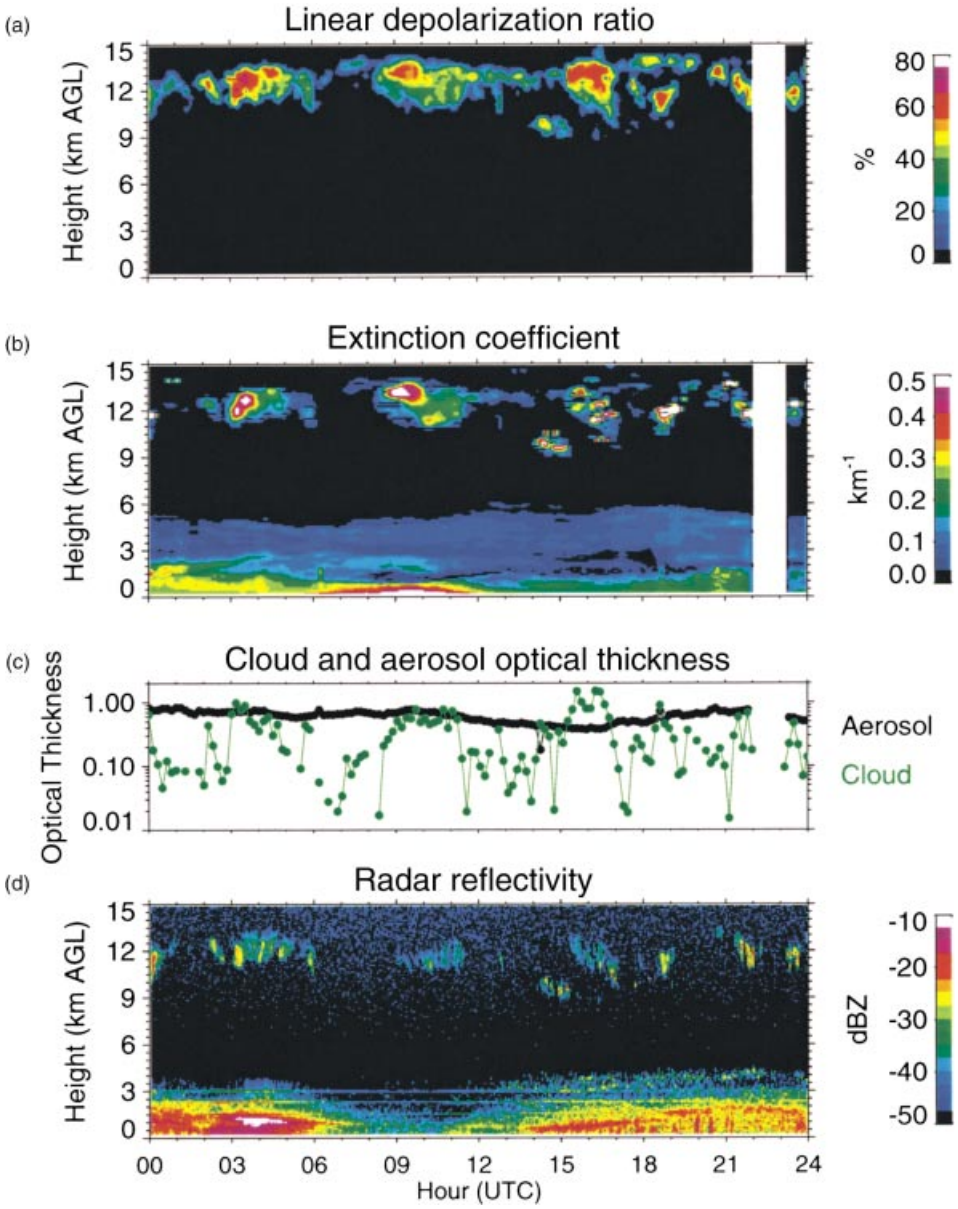

Figure 17. Time–height cross-section of linear depolarization ratio from the CART Raman lidar (a), extinction in both clouds and aerosols (b), optical thickness from clouds (green) and aerosols (black) (c) integrated from the extinction data, and reflectivity data from the co-located millimeter cloud radar (MMCR) at the CART site (d). See text for details.

5.7 Cloud properties

Clouds greatly impact the radiative transfer through the atmosphere. Depending on composition and location, they can serve to cool the earth–atmosphere system by reflecting large amounts of incoming solar radiation back to space, or warm the system by absorbing outgoing radiation and thus reducing the rate at which energy escapes the atmosphere. There are many important parameters that are needed to account for clouds in radiative transfer and climate models, and Raman lidars have proven to be a valuable source of many of these parameters.[35,53,63]

The CARL's laser transmits polarized light, and elastic backscatter (i.e. at the laser's wavelength) is separated into the two polarizations with electric-field vectors either parallel or perpendicular to the electric-field vector of the outgoing laser beam. The ratio of these two signals is the linear depolarization ratio, which is very sensitive to the shape of the scatterer. Ice particles induce some degree of depolarization, while cloud water droplets, which are typically spherical (unless they are falling at a relatively fast rate), will induce a negligible amount of depolarization. Therefore, the depolarization ratio provides information on the phase of clouds, and is very sensitive to thin

clouds composed of ice. Sassen provided an extensive review of the polarization lidar technique.[91] A time–height cross-section of the linear depolarization ratio of a pervasive cirrus event over the CART site as measured by the Raman lidar on 30 May 1998 is given in Figure 17(a). During this day-long event, the cirrus layer ranged from less than 1 km to almost 4 km in geometric thickness, and the depolarization values in the layer varied significantly from values of less than 10% to over 60%. The temporal resolution of the depolarization data is 10 min.

Since this lidar is able to measure extinction, the extinction in the cirrus layer was calculated (Figure 17b). The temporal resolution of the extinction data is 30 min, to reduce the random error. Areas with higher values of depolarization appear to correlate with higher values of extinction, but the correlation is not perfect. Note that the extinction in the clouds is much more variable over time than the extinction in the aerosol layer below 6 km, which is also shown in the optical thickness plot in Figure 17(c). The high values of the aerosol extinction in the lowest 6 km (and high aerosol optical depths) is probably due to advection of smoke from the fires in Central America. This event has been discussed in detail.[92] Multiple scattering of the laser radiation by the cloud particles, which tends to decrease the apparent optical depth,[63,64] has not been accounted for in these calculations.

This cirrus layer presented in Figure 17 remained relatively thin (i.e. optical depths less than 2) compared with typical stratus clouds, hence the laser beam was not fully extinguished while passing through the cloud. However, clouds with an optical depth much larger than 2–3 will attenuate the laser beam before it exits the cloud, hence the upper portion of the cloud will not be sensed by the lidar. Attenuation does not affect the MMCR at the SGP CART site[93] except during periods of precipitation. However, owing to its 8-mm wavelength, the MMCR is insensitive to small hydrometeors, even in its most sensitive mode,[94] whereas the lidar is not. Figure 17(d) shows the reflectivity from the MMCR's most sensitive pulse-coded cirrus mode. Note that the strong return from the radar in the lowest 4 km is not due to hydrometeors, but rather are returns from insects and other atmospheric "plankton".[95] Also, the horizontal striping in the lowest 3 km in the radar data is caused by artifacts due to the pulse coding, which is used to increase the sensitivity of the MMCR at high altitudes. In this case, the MMCR is insensitive to the cirrus layer for a large fraction of the day owing to the small particles in the layer. However, given the MMCR's ability to profile through optically thick layers and the lidar's ability to detect thin layers, Clothiaux *et al.* devised an algorithm that merges together the two data streams to derive the best estimate of the cloud location.[95] Lidars are a critical part of a robust cloud detection algorithm to define cloud base and layers accurately with very small hydrometeors. Raman lidars, given their ability to measure elastic backscatter, extinction, and humidity simultaneously, are better than single-wavelength lidars able to define cloud base or the presence of virga.[96] Also, new techniques are being developed to take advantage of the different sensitivities of radars and lidars to retrieve microphysical cloud properties.[97]

The Raman lidar cloud boundary and cloud optical depth data, when used in conjunction with observations from an IR radiometer, can be used to retrieve optical properties from cirrus clouds in both the IR and ultraviolet (UV) regions.[98,99] One advantage of using a water vapor Raman lidar such as CARL over a single-wavelength elastic backscatter lidar is that the Raman lidar is able to measure directly the water vapor below the cloud, which contributes significantly to the emitted radiance observed by the IR radiometer. This allows the emission from the cloud can be determined more accurately.

6 THE FUTURE

There are several new developments on the horizon that will benefit Raman lidars, and atmospheric science in general. The development of the first truly operational Raman lidar at the ARM CART site will be followed with more automated systems. These new systems will become smaller, less expensive, and easier to deploy, and will greatly increase the high temporal and spatial resolution of the water vapor, aerosol, and cloud distribution data in our atmosphere. This will lead to a large increase in the understanding of the subgrid-scale processes that affect the weather and climate, which will improve the parameterizations in the models used to predict weather and climate.

Another ongoing area of research is in the absolute calibration of Raman lidars. The largest uncertainty in the absolute calibration of Raman lidars is the uncertainty in the Raman cross-section for water vapor.[39] This has necessitated the practice of calibrating a Raman water vapor lidar with respect to another sensor such as a radiosonde or microwave radiometer. There have been several efforts to establish an absolute calibration for Raman lidars that does not require the use of a water vapor measurement by another instrument.[69,100] We are attempting to improve the knowledge of the ratio of the water vapor to nitrogen Raman cross-sections by using the demonstrated calibration stability of CARL with respect to a source considered accurate, in absolute terms. This holds the potential for reducing the uncertainty in the calibration of any Raman lidar system to $\pm 3\%$ given an accurate radiometric calibration of the lidar.

Another new development in the field of water vapor Raman lidars is the development of an airborne Raman lidar system capable of both day- and night-time measurements of water vapor and other parameters. To date, only night-time water vapor measurements have been made from an airborne platform. A modeling study has shown that an airborne Raman lidar looking down offers a significant performance increase compared with the same system looking upward from the ground during both the night and the day.[101] This performance increase is a combination of natural signal compression due to the increase in water vapor (and hence in Raman backscatter due to water vapor molecules) further away from the instrument when looking downward and a reduced solar background due to the viewing direction. A downward-looking day/night water vapor system based upon these model results is currently under construction.

7 SUMMARY

The inelastic scattering that Chandrasekhara Raman first discovered has proven to be invaluable for a wide variety of laser-based remote sensing applications. The laser and detection technologies have advanced markedly over the last 30 years, and the first truly automated turn-key Raman lidar for the profiling of atmospheric water vapor, aerosols, and clouds has been built and deployed. Data from this system and other Raman lidars have greatly advanced the knowledge of the fine-scale structure and evolution of the atmosphere, and continue to play an important role in atmospheric research. Raman lidars have the capability to specify completely the state of the atmosphere remotely, and when teamed together with other instruments, including in situ and remote sensors, provide unparalleled information about the nature and structure of the atmosphere and its components.

ABBREVIATIONS AND ACRONYMS

AERI	Atmospheric Emitted Radiance Interferometer
AOT	Aerosol Optical Thickness
ARM	Atmospheric Radiation Measurement
CARL	Cloud and Radiation Testbed Raman Lidar
CART	Cloud and Radiation Testbed
DIAL	Differential Absorption Lidar
FOV	Field-of-view
GMT	Greenwich Mean Time
HSRL	High Spectral Resolution Lidar
HVAC	Heating, Ventilation, and Air Conditioning
lidar	Light Detection and Ranging
MMCR	Millimeter Cloud Radar
MWR	Microwave Radiometer
Nd : YAG	Neodymium-doped Yttrium Aluminum Garnet
OLR	Outgoing Longwave Radiation
PWV	Total Precipitable Water Vapor
RH	Relative Humidity
UPS	Uninterruptible Power Supply
UTC	Universal Time Coordinates

REFERENCES

1. C.D. Ahrens, 'Meteorology Today: an Introduction to Weather, Climate, and the Environment', 5th edition, West Publishing, St Paul, MN (1994).
2. W.P. Menzel, F.C. Holt, T.J. Schmidt, R.M. Aune, A.J. Schreiner, G.S. Wade and D.G. Gray, *Bull. Am. Meterol. Soc.*, **79**, 2059 (1998).
3. Y. Han and E.R. Westwater, *J. Atmos. Oceanic Technol.*, **12**, 1050 (1995).
4. W.F. Feltz, W.L. Smith, R.O. Knuteson, H.E. Revercomb, H.M. Woolf and H.B. Howell, *J. Appl. Meteorol.*, **37**, 857 (1998).
5. V. Wulfmeyer and J. Bösenberg, *Appl. Opt.*, **37**, 3825 (1998).
6. W.B. Grant, *Opt. Eng.*, **30**, 40 (1991).
7. D.D. Turner, H. Linné, J. Bösenberg, S. Lehmann, K. Ertel, J.E.M. Goldsmith and T.P. Tooman, 'Simultaneous Ground-based Remote Sensing of Water Vapor by Differential Absorption and Raman Lidars', in "Proceedings of the IEEE International Geoscience and Remote Sensing Symposium (IGARSS 2000), Honolulu, HI", ed. T. Stein, IEEE, Piscataway, NJ, 1455–1458 (2000).
8. H. Linné, D.D. Turner, J.E.M. Goldsmith, T.P. Tooman, J. Bösenberg, K. Ertel and S. Lehmann, 'Intercomparison of DIAL and Raman Lidar Measurements of Humidity Profiles', in "Advances in Laser Remote Sensing. Selected papers presented at the 20th International Laser Radar Conference, Vichy, France, 10–14 July 2000", eds A. Dobas, C. Loth and J. Pelon, Ecole Polytechnique, Palaiseau, France (2001).
9. A. Anderson (ed.), 'The Raman Effect', Marcel Dekker, New York (1971).
10. E.O. Hulburt, *J. Opt. Soc. Am.*, **27**, 377 (1937).
11. L. Elterman, *J. Geophys. Res.*, **58**, 519 (1953).
12. T.H. Maiman, *Nature (London)*, **187**, 493 (1960).
13. L.D. Smullin and G. Fiocco, *Nature (London)*, **94**, 1267 (1962).
14. F.J. McClung and R.W. Hellwarth, *J. Appl. Phys.*, **33**, 828 (1962).
15. G. Fiocco and L.D. Smullin, *Nature (London)*, **199**, 1275 (1963).
16. R.M. Schotland, 'Some Observations of the Vertical Profile of Water Vapor by Means of a Laser Optical Radar', presented at the Fourth Symposium on Remote Sensing of the Environment, April (1966).

17. M.R. Bowman, A.J. Gibson and M.C.W. Sandford, *Nature (London)*, **22**, 456 (1969).
18. J.A. Cooney, *Appl. Phys. Lett.*, **12**, 40 (1968).
19. D.A. Leonard, *Nature (London)*, **216**, 142 (1967).
20. H. Inaba and T. Kobayasi, *Nature (London)*, **224**, 170 (1969).
21. H. Inaba and T. Kobayasi, *Opto-electronics*, **4**, 101 (1972).
22. B. Caputo, D.A. Leonard and J. Guagliardo, *Opt. Spectra*, **14**, 57 (1980).
23. S.H. Melfi, J.D. Lawrence, Jr and M.P. McCormick, *Appl. Phys. Lett.*, **15**, 295 (1969).
24. J.A. Cooney, *J. Appl. Meteorol.*, **9**, 182 (1970).
25. W.F. Murphy, W. Holzer and H.J. Berstein, *Appl. Spectrosc.*, **23**, 211 (1969).
26. V.E. Derr and C.G. Little, *Appl. Opt.*, **9**, 1976 (1970).
27. C.M. Penney and M. Lapp, *J. Opt. Soc. Am.*, **66**, 422 (1976).
28. J.A. Cooney, *Spectrosc. Lett.*, **3**, 305 (1971).
29. S.H. Melfi, *Appl. Opt.*, **11**, 1605 (1972).
30. R.G. Strauch, V.E. Derr and R.E. Cupp, *Remote. Sens. Environ.*, **2**, 101 (1972).
31. J.C. Pourney, D. Renaut and A. Orszag, *Appl. Opt.*, **13**, 1141 (1979).
32. D. Renault, J.C. Pourney and R. Capitini, *Opt. Lett*, **5**, 233 (1980).
33. S.H. Melfi and D.N. Whiteman, *Bull. Am. Meteorol. Soc.*, **66**, 1288 (1985).
34. J.E.M. Goldsmith, F.H. Blair, S.E. Bisson and D.D. Turner, *Appl. Opt.*, **37**, 4979 (1998).
35. D.N. Whiteman and S.H. Melfi, *J. Geophys. Res.*, **104**, 31 411 (1999).
36. D.A. Leonard, B. Caputo and R.L. Johnson, *Geophys. Res. Lett.*, **4**, 279 (1977).
37. G. Cecchi and V. Raimondi, *Proc. SPIE*, **2959**, 208 (1997).
38. M. Becucci, S. Cavalieri, R. Eramo, L. Fini and M. Materazzi, *Appl. Opt.*, **38**, 928 (1999).
39. G. Vaughan, D.P. Waring, L. Thomas and V. Mitev, *Q. J. R. Meteorol. Soc.*, **114**, 1471 (1988).
40. O.A. Bukin, 'Application of Raman Spectroscopy for Diagnostic of Atmospheric Water in Gas and Liquid State', PhD Dissertation., Institute of Oceanology, Vladivostok (1985).
41. S.H. Melfi, K.D. Evans, J. Li, D.N. Whiteman, R.A. Ferrare and G.K. Schwemmer, *Appl. Opt.*, **36**, 3551 (1997).
42. P. Keckhut, M.-L. Chanin and A. Hauchecorne, *Appl. Opt.*, **29**, 5182 (1990).
43. A. Hauchecorne and M.-L. Chanin, *Geophys. Res. Lett.*, **7**, 565 (1980).
44. J.A. Salzman and T.A. Coney, 'Remote Measurement of Atmospheric Temperatures by Raman Lidar', NASA Technical Memorandum TM X-68250, NASA, Washington, DC (1973).
45. G. Vaughan, D.P. Wareing, S.J. Pepler, L. Thomas and V. Mitev, *Appl. Opt.*, **32**, 2758 (1993).
46. D. Nedeljkovic, A. Hauchecorne and M.-L. Chanin, *IEEE Trans. Geosci. Remote. Sens.*, **31**, 90 (1993).
47. P.A.T. Haris, 'Pure Rotational Raman Lidar for Temperature Measurements in the Lower Troposphere', PhD Dissertation, Pennsylvania State University (1995).
48. U. Wandinger, I. Mattis, A. Ansmann, Y. Arshinov, S. Bobrovnikov and I. Serikov, 'Tropospheric Temperature Profiling Based on Detection of Stokes and Anti-Stokes Rotational Raman Lines at 532 nm', in "Proceedings of the 19th International Laser Radar Conference", ed. U.N. Singh, NASA Conference Publication 207671, Part 1, NASA, Washington, DC, 297–300 (1998).
49. C.J. Grund and E.W. Eloranta, *Opt. Eng.*, **30**, 6 (1991).
50. S.T. Shipley, D.H. Tracy, E.W. Eloranta, J.T. Trauger, J.T. Sroga, F.L. Roesler and J.A. Weinman, *Appl. Opt.*, **22**, 3716 (1983).
51. A. Ansmann, M. Eiebesell and C. Weitkamp, *Opt. Lett*, **15**, 746 (1990).
52. R.A. Ferrare, S.H. Melfi, D.N. Whiteman and K.D. Evans, *Geophys. Res. Lett.*, **19**, 1599 (1992).
53. A. Ansmann, U. Wandinger, M. Riebesell, C. Weitkamp and W. Michaelis, *Appl. Opt.*, **31**, 7113 (1992).
54. R.A. Ferrare, S.H. Melfi, D.N. Whiteman, K.D. Evans and R. Leifer, *J. Geophys. Res.*, **103**, 19 663 (1998).
55. T.J. McGee, M. Gross, R. Ferrare, W. Heaps and U. Singh, *Geophys. Res. Lett.*, **20**, 955 (1993).
56. F. Balsinger and C.R. Philbrick, *Proc. SPIE*, **2833**, 231.
57. R.M Measures, 'Laser Remote Sensing: Fundamentals and Applications', Wiley, New York (1984).
58. D.N. Whiteman, W.F. Murphy, N.W. Walsh and K.D. Evans, *Opt. Lett*, **18**, 247 (1993).
59. D.D. Turner and J.E.M. Goldsmith, *J. Atmos. Oceanic Technol.*, **16**, 1062 (1999).
60. D.N. Whiteman, S.H. Melfi and R.A. Ferrare, *Appl. Opt.*, **31**, 3068 (1992).
61. D.D. Turner, R.A. Ferrare, L.A. Heilman, W.F. Feltz and T.P. Tooman, *J. Atmos. Oceamic Technol.*, submitted (2001).
62. D.N. Whiteman, *Appl. Opt.*, **38**, 3360 (1999).
63. D.N. Whiteman, K.D. Evans, B. Demoz, D.O'C. Starr, D. Tobin, W. Feltz, E.W. Eloranta, G.J. Jedlovec, S.I. Gutman, G.K. Schwemmer, M. Cadirola, S.H. Melfi and F. Schmidlin, *J. Geophys. Res.*, in press (2001).
64. E.W. Eloranta, *Appl. Opt.*, **37**, 2464 (1998).
65. R.G. Ellingson and Y. Fouquart, *J. Geophys. Res.*, **96**, 8925 (1991).
66. G.M. Stokes and S.E. Schwartz, *Bull. Am. Meteorol. Soc.*, **75**, 1201 (1994).
67. J.E.M. Goldsmith and R.A. Ferrare, 'Performance Modeling of Daytime Raman Lidar Systems for Profiling Atmospheric Water Vapor', in "Proceedings of the 16th International Laser Radar Conference, NASA Conference Publication 3158, Part 2, NASA, Washington, DC, 667–670 (1992).
68. D. Renault and R. Capitini, *J. Atmos. Oceanic Technol.*, **5**, 585 (1988).

69. S.E. Bisson, J.E.M. Goldsmith and M.G. Mitchell, *Appl. Opt.*, **38**, 1841 (1999).
70. J. Wessel, S. Beck, Y. Chan, R. Farley and J. Gelbwachs, *IEEE Trans. Geosci. Remote Sens.*, **31**, 141 (1999).
71. R.A. Ferrare, S.H. Melfi, D.N. Whiteman, K.D. Evans, F.J. Schmidlin and D.O'C. Starr, *J. Atmos. Oceanic Technol.*, **12**, 1177 (1995).
72. D.D. Turner, T.R. Shippert, P.D. Brown, S.A. Clough, R.O. Knuteson, H.E. Revercomb and W.L. Smith, 'Long-term Analysis of Observed and Line-by-line Calculations of Longwave Surface Spectral Radiance and the Effect of Scaling the Water Vapor Profiles', in "Proceedings of the Eighth Atmospheric Radiation Measurement (ARM) Science Team Meeting, Tucson, AZ" (1998). Available from http://www.arm.gov/pub/docs/documents/technical/conf_9803/turner-98.pdf.
73. E.J. Zipser and R.H. Johnson, 'Systematic Errors in Radiosonde Humidities: a Global Problem?', in "Preprints of the 10th Symposium on Meteorological Observations and Instrumentation, Phoenix, AZ", American Meteorological Society, Boston, MA, 72–73 (1998).
74. E.R. Miller, J. Wang and H.L. Cole, 'Correction for Dry Bias in Vaisala Radiosonde RH Data', in "Proceedings of the Ninth Atmospheric Radiation Measurement (ARM) Science Team Meeting, Tucson, AZ" (1999). Available from http://www.arm.gov/pub/docs/documents/technical/conf_9903/miller-er-99.pdf.
75. S.A. Clough, P.D. Brown, D.D. Turner, T.R. Shippert, J.C. Liljegren, D.C. Tobin, H.E. Revercomb and R.O. Knuteson, 'Effect on the Calculated Spectral Surface Radiances Due to MWR Scaling of Sonde Water Vapor Profiles', in "Proceedings of the Ninth Atmospheric Radiation Measurement (ARM) Science Team Meeting, San Antonio, TX" (1999). Available from http://www.arm.gov/pub/docs/documents/technical/conf_9903/clough-99.pdf.
76. D.D. Turner, W.F. Feltz and R.A. Ferrare, *Bull. Am. Meteorol. Soc.*, **81**, 1301 (2000).
77. J.C. Liljegren and B.M. Lesht, 'Measurements of Integrated Water Vapor and Cloud Liquid Water from Microwave Radiometers at the DOE ARM Cloud and Radiation Testbed in the U.S. Southern Great Plains', in "Proceedings of the International Geoscience and Remote Sensing Symposium (IGARSS), Lincoln, NB", ed. T. Stein, IEEE, Piscataway, NJ, 1675–1977 (1996).
78. K.D. Evans, S.H. Melfi, R.A. Ferrare and D.N. Whiteman, *Appl. Opt.*, **36**, 2594 (1997).
79. W.L. Smith, W.F. Feltz, R.O. Knuteson, H.E. Revercomb, H.B. Howell and H.M. Woolf, *J. Atmos. Oceanic Technol.*, **16**, 323 (1999).
80. C.D. Whiteman, X. Bian, S. Zhong and J.C. Liljegren, 'Moisture Transport by the Low-level Jet', in "Proceedings of the Sixth Atmospheric Radiation Measurement (ARM) Science Team Meeting, San Antonio, TX" (1996). Available from http://www.arm.gov/pub/docs/documents/technical/conf_9603/white_96.pdf.
81. W.E. Eichinger, D.I. Cooper, P.R. Forman, J. Griegos, M.A. Osborn, D. Richter, L.L. Tellier and R. Thornton, *J. Atmos. Oceanic Technol.*, **16**, 1753 (1999).
82. W.L. Ecklund, D.A. Carter and B.B. Balsley, *J. Atmos. Oceanic Technol.*, **5**, 432 (1988).
83. S.H. Melfi, D.N. Whiteman and R.A. Ferrare, *J. Appl. Meteorol.*, **28**, 789 (1989).
84. B. Demoz, K.D. Evans, D. Starr, D.N. Whiteman, G.K. Schwemmer and D.D. Turner, 'Raman Observations of Lifting at a Convergence Line', in "Advances in Laser Remote Sensing. Selected papers presented at the 20th International Laser Radar Conference, Vichy, France, 10–14 July 2000", eds A. Dobas, C. Loth and J. Pelon, Ecole Polytechnique, Palaiseau, France (2001).
85. C. Pilinis, S.N. Sandis and J.H. Seinfeld, *J. Geophys. Res.*, **100**, 18 739 (1995).
86. V. Wulfmeyer and G. Feingold, *J. Geophys. Res.*, **105**, 4729 (2000).
87. K.P. Shine and A. Sinda, *Nature (London)*, **354**, 382 (1991).
88. B.J. Soden, S.A. Ackerman, D.O'C. Starr, S.H. Melfi and R.A. Ferrare, *J. Geophys. Res.*, **99**, 21 005 (1994).
89. E.J. Mlawer, S.J. Taubman, P.D. Brown, M.J. Iacono and S.A. Clough, *J. Geophys. Res.*, **102**, 16 663 (1997).
90. S.H. Melfi, D.D. Turner, K.D. Evans, D.N. Whiteman, G.K. Schwemmer and R.A. Ferrare, 'Upper Tropospheric Water Vapor: a Field Campaign of two Raman Lidars, Airborne Hygrometers, and Radiosondes', in "Proceedings of the 19th International Laser Radar Conference, Annapolis, MD", eds U. Singh, S. Ismail and G. Schwemmer, National Aeronautics and Space Administration, Hampton, VA, 367–370 (1998).
91. K. Sassen, *Bull. Am. Meteorol. Soc.*, **72**, 1848 (1991).
92. R.A. Peppler, L. Ashford, C.P. Bahrmann, J.C. Barnard, R.A. Ferrare, R.N. Halthore, N.S. Laulainen, J.A. Ogren, M.R. Poellot, M.E. Splitt and D.D. Turner, *Bull. Am. Meterol. Soc.*, **81**, 2563 (2000).
93. K.P. Moran, B.E. Martner, M.J. Post, R.A. Kropfli, D.C. Welsh and K.B. Widener, *Bull. Am. Meteorol. Soc.*, **79**, 443 (1998).
94. E.E. Clothiaux, K.P. Moran, B.E. Martner, T.P. Ackerman, G.G. Mace, T. Uttal, J.H. Mather, K.B. Widener, M.A. Miller and D.J. Rodriguez, *J. Atmos. Oceanic Technol.*, **16**, 819 (1999).
95. E.E. Clothiaux, T.P. Ackerman, G.G. Mace, K.P. Moran, R.T. Marchand, M.A. Miller and B.E. Martner, *J. Appl. Meteorol.*, **39**, 645 (2000).
96. B. Demoz, D. Starr, D.N. Whiteman, K.D. Evans, D. Hlavka and R. Peravali, *Geophys. Res. Lett.*, **27**, 1899 (2000).
97. D.P. Donovan and A.C.A.P. Lammeren, *Phys. Chem. Earth (B)*, **25**, 115 (2000).
98. C.M.R. Platt, *J. Appl. Meteorol.*, **18**, 1130 (1979).
99. C.M.R. Platt, S.A. Young, P.J. Manson, G.R. Patterson, S.C. Marsden, R.T. Austin and J. Churnside, *J. Atmos. Sci.*, **55**, 1977 (1998).
100. V. Sherlock, A. Hauchecorne and J. Lenoble, *Appl. Opt.*, **38**, 5816 (1999).
101. D.N. Whiteman, G. Schwemmer, T. Berkoff, H. Plotkin, L. Ramos-Izquierdo and G. Pappalardo, *Appl. Opt.*, **40**, 375 (2001).